Quaternary Science Reviews 318 (2023) 108287

Contents lists available at ScienceDirect

Quaternary Science Reviews

journal homepage: www.elsevier.com/locate/quascirev

Last interglacial global mean sea level from high-precision U-series ages of Bahamian fossil coral reefs

Oana A. Dumitru [a,*], Blake Dyer [b], Jacqueline Austermann [a,c], Michael R. Sandstrom [a,c], Steven L. Goldstein [a,c], William J. D'Andrea [a], Miranda Cashman [a,c], Roger Creel [a], Louise Bolge [a], Maureen E. Raymo [a,c]

[a] Lamont-Doherty Earth Observatory, Columbia University, Palisades, NY, 10964, USA
[b] School of Earth and Ocean Sciences, University of Victoria, Victoria, BC, Canada
[c] Department of Earth and Environmental Sciences, Columbia University, Palisades, NY, 10964, USA

ARTICLE INFO

Handling Editor: C. Hillaire-Marcel

Keywords:
Last interglacial
U-series ages
The Bahamas
Sea-level changes

ABSTRACT

Accurate characterization of Last Interglacial (MIS 5e; ~129–116 ka) sea level is important for understanding ice sheet sensitivity to climate change, with implications for predicting future sea-level rise. Here we present a record of MIS 5e sea level based on high-precision U-series ages of 23 corals with precise elevation measurements from reefs around Crooked Island, Long Cay, Long Island, and Eleuthera, The Bahamas. Rigorous screening criteria identified the most pristine samples, and nearly all samples show a narrow $\delta^{234}U_{initial}$ range between 143.8 and 151.3‰. We infer global mean sea level (GMSL) from these local observations by correcting them for glacial isostatic adjustment (GIA) and long-term subsidence. For GIA, we consider a range of ice histories and Earth viscosity structures. We identify, via Bayesian inference, the range of isostatic and GMSL histories that are consistent with MIS 5e observations across The Bahamas. When applying an open-system correction to our ages, we find that MIS 5e GMSL likely peaked higher than 1 m, but very unlikely exceeded 2.7 m. Our posterior GMSL is lower than previous estimates, but consistent with recent results of modeling and observations. Additionally, sea level observations at other locations (Seychelles, Western Australia, Yucatan) are only slightly above/within the 95% range of predicted local sea level, i.e., GIA plus GMSL, for our open-system/closed-system results. Our relatively constant MIS 5e GMSL indicates that Greenland and Antarctica melted beyond their present extents and, given the insolation forcing, that their contributions to GMSL were likely out-of-phase. These results indicate that the ice sheets may be very sensitive to regional temperature, which has important implications for their combined impact on global sea levels at a time when greenhouse gases increases are causing simultaneous warming at both poles.

1. Introduction

Substantial sea-level rise is projected by the end of the 21st century under almost all climate-warming scenarios (Garbe et al., 2020; Horton et al., 2020). However, the amount that the present-day Greenland (GrIS) and Antarctic (AIS) ice sheets will melt in the coming decades to centuries, and the speed of that melt, remains uncertain (Fox-Kemper et al., 2021; Pattyn et al., 2018; Slater et al., 2020). To calibrate ice sheet models used to constrain the future stability of the GrIS and AIS and the corresponding sea-level rise, scientists draw on evidence from past interglacial periods when Earth's climate was hotter than today (DeConto and Pollard, 2016; Fischer et al., 2018). The Last Interglacial (Marine Isotope Stage (MIS) 5e; ~129–116 thousand years ago, ka) is an important calibration target because global mean surface temperatures were similar or slightly higher than today and comparable with low-end 21st century projections (0.5–1.5 °C higher than pre-industrial values (Fox-Kemper et al., 2021)). Knowledge of sea-level change during MIS 5e can therefore provide valuable insight into likely patterns of future sea-level rise (Gilford et al., 2020; IPCC, 2013).

Yet the timing, magnitude, and evolution of sea-level change during MIS 5e are subjects of ongoing debate. Common MIS 5e global mean sea level (GMSL) scenarios include one early (Dutton et al., 2015; Polyak et al., 2018) or late (O'Leary et al., 2013; Stocchi et al., 2018) sea-level peak, two peaks (Kopp et al., 2009), or multiple sea-level highstands

* Corresponding author.
E-mail address: odumitru@ldeo.columbia.edu (O.A. Dumitru).

https://doi.org/10.1016/j.quascirev.2023.108287
Received 6 March 2023; Received in revised form 23 August 2023; Accepted 24 August 2023

(Thompson et al., 2011; Thompson and Goldstein, 2005). Major difficulties in resolving this debate include finding pristine MIS 5e sea-level indicators and a deficiency in our understanding of Earth deformation processes, such as glacial isostatic adjustment (GIA) and dynamic topography, which alter local sea level relative to the global mean (Austermann et al., 2017; Dendy et al., 2017; Raymo et al., 2011). Previous GMSL estimates had been converging on values of 5–10 m above present sea level (Dutton et al., 2015; Dutton and Lambeck, 2012; Fox-Kemper et al., 2021; Kopp et al., 2009 and references therein). However, recent reconstructions based on both observations and ice sheet modeling suggest that MIS 5e GMSL might have been lower than this range (Clark et al., 2020; Dyer et al., 2021; Polyak et al., 2018). These recent results imply that polar ice sheets may have been less susceptible to melting than previously thought, or, as we propose here, that Antarctica and Greenland were out-of-phase with one another during this time interval, a pattern also suggested by others (i.e., Dyer et al., 2021; Rohling et al., 2019). Here we present a set of well-dated sea-level records that provide more accurate estimates for the magnitude and timing of MIS 5e GMSL, which can be used to test and calibrate ice-sheet models and ultimately to improve projections of the sea-level rise by 2100 and beyond.

The Bahamian Archipelago is an excellent place to study sea-level changes during MIS 5e because i) it is an area experiencing minimal tectonic activity (Carew and Mylroie, 1995), where long-term subsidence can be constrained using subsurface core data (McNeill, 2005); ii) the islands form a transect across the southeastern edge of the Laurentide ice sheet peripheral bulge, and hence variations in relative sea level across the archipelago caused by GIA can be used to constrain mantle viscosity and past ice history (Dyer et al., 2021); iii) different types of sedimentary deposits that accumulated on these carbonate islands provide an excellent record of past sea-level fluctuations (Chen et al., 1991; Hearty et al., 2007; Muhs et al., 2020; Skrivanek et al., 2018; Thompson et al., 2011); and iv) some of these sea-level indicators can be dated precisely using radiometric methods.

The majority of extant MIS 5e relative sea-level estimates from The Bahamas are obtained using fossil coral reefs. A total of 200 U-series ages from 142 unique coral specimens sampled from emergent MIS 5e reef deposits on Abaco Island (Hearty et al., 2007), New Providence (Muhs et al., 2020), Great Inagua, and San Salvador (McNeill, 2005; Skrivanek et al., 2018; Thompson et al., 2011) have been compiled by Chutcharavan and Dutton (2021). Unfortunately, coral skeletal material is highly susceptible to post-depositional alteration, particularly after exposure to seawater or meteoric water flow (e.g., Thompson et al., 2003). Therefore, the U-series measurements must be carefully evaluated before they can be used to constrain a fossil coral age. Applying strict geochemical screening criteria to remove data that have been altered through open-system behavior (corals that gained or lost uranium and thorium since the deposition time; Chutcharavan and Dutton, 2021; Dutton and Lambeck, 2012; Hibbert et al., 2016; Scholz and Mangini, 2007) has resulted in the rejection of the vast majority of published U-series data. Hence, more robust chronologies of Bahamian fossil corals, which can constrain GIA model parameters and reduce the uncertainty in inferred GMSL, are needed. In this paper we add to the database and present the first high-precision U-series ages of fossil corals, along with detailed elevation measurements, from Crooked Island, Long Cay, Long Island, and Eleuthera. We provide: i) a reconstruction of relative sea level (RSL) based on detailed field observations with precise elevation measurements and reliable high-precision U–Th ages from islands that have not been previously explored for this purpose. We only include in our analysis fossil corals that were found in growth position and passed a strict preservation screening criteria (detailed in Materials and Methods) which allows us to provide a high-quality set of U-series data; ii) an interpretation of these local data in terms of GMSL by correcting for both GIA and long-term subsidence. One major difference between our analysis and previous studies is an extensive assessment of GIA, which includes a large suite of viscosity structures and a variety of MIS 6 ice configurations. Combining our new results with existing data allows us to better constrain GMSL during MIS 5e and evaluate whether or not it oscillated; iii) we take this analysis a step further and draw inferences, based on the GMSL results, for the sources of MIS 5e sea-level high-stand. Lastly, as we build on the approach of Dyer et al. (2021), our work constitutes a test of their results with new independent data, which adds more confidence to their model.

2. Materials and Methods

2.1. Geologic setting of the surveyed islands, sample location and elevation

The Bahamian archipelago includes over 700 islands and cays that extend for more than 1000 km along a northwest-southeast trend, from Florida to the Greater Antilles (Fig. 1a). The islands are dominated by two landforms accumulated during MIS 5e: aeolian dunes deposited above sea level, and extensive limestone flats that precipitated underwater and exhibit marine features including corals, herringbone cross-stratification, coated grains, and subtidal trace fossils (Dyer et al., 2021; Garrett and Gould, 1984; Mylroie, 2008). Fossil corals dated to the Last Interglacial period are found on platform edge reefs, in lagoonal patch reefs up to 10 m wide, and as isolated corals on the flanks of lithified dunes. The islands have a diversity of depositional environments, with higher energy features, such as barrier reefs, more common on the windward margin (east), and muddy mangrove-filled tidal creeks more common on the leeward margin (west; Berkeley and Rankey (2012); Shinn et al. (1969)).

In this work we present new observations and dates from Crooked Island, Long Cay, Long Island, and Eleuthera, which are less explored compared to the more populated and accessible cays, such as New Providence (Garrett and Gould, 1984; Hearty and Pascal, 1997; Muhs et al., 2020) and San Salvador (Chen et al., 1991; Skrivanek et al., 2018; Thompson et al., 2011). *Crooked Island*, with an area of 197 km^2 and trending roughly E–W, is located in the southeastern part of the Bahamian archipelago (Fig. 1A). The island is composed of low-lying marine deposits that include coral rubble and in situ reefs, subtidal sands, burrowed facies. Godefroid and Kindler (2015) reported four prominent geologic units on Crooked Island that preserve carbonates from the early Pleistocene through the Holocene. *Long Cay* is an extension of the western arm of Crooked Island, separated from it by a channel. Together with Acklins Island and an interior lagoon, Crooked Island and Long Cay define the Bight of Acklins (Godefroid and Kindler, 2015). Northwest of Crooked Island lies *Long Island*, a narrow landmass 130 km long and not wider than 15 km (Fig. 1D). The island of *Eleuthera,* roughly 177 km long and less than 3 km wide (Kindler et al., 2010), is located on the northeastern margin of Great Bahama Bank, its windward site facing the Atlantic (Fig. 1E). Well-developed shelf-edge coral framework and scattered lagoonal and dune corals from the last interglacial have been previously mapped throughout the Bahamas, including on Crooked Island (Godefroid and Kindler, 2015) and Eleuthera (Hearty and Kindler, 1993a,b). We identified analogous units throughout Long Cay and Long Island.

We conducted campaigns in 2016, 2017, and 2019 to survey elevations of fossil corals and collected samples for U-series dating. We sampled corals only from the surface of the outcrop (none in vertical section) and, whenever possible, we collected samples at the highest elevation at each site. To get insight into which locations might contain MIS 5e fossil corals, we combined open access 3-m resolution digital elevation models from the TanDEM-X mission (Fig. 1) with field observations of the major morphostratigraphic features (e.g., dunes, lagoons, strand plains, and exposed reefs). Once emergent fossil corals were found, we selected in situ corals (none of our samples has been eroded or truncated) for sampling and measured their elevations at the uppermost surface of the coral heads using high-precision differential GPS measurements (for details on the outcrop surveys and vertical

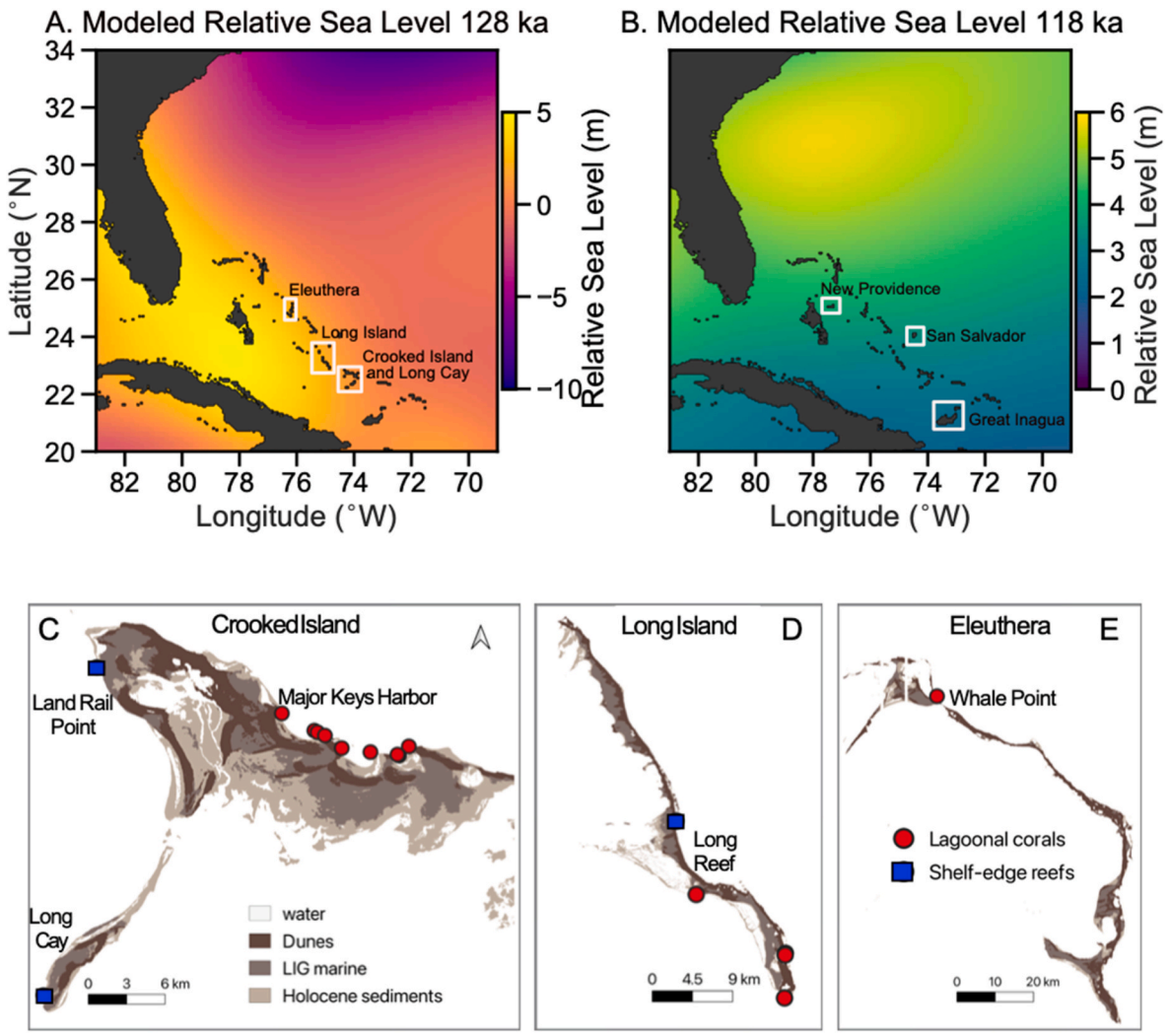

Fig. 1. A) and B) Modeled RSL that best fits the observations (the weighted average of the posterior RSL) near the start and end of MIS 5e, respectively, assuming no change in GMSL during MIS 5e (i.e., all changes driven by GIA). White squares indicate the location of the islands from which corals were dated for this study (A) and previously published work (B). C), D), and E) Geologic maps of Crooked Island and Long Cay, Long Island, and Eleuthera, respectively, showing where MIS 5e corals were sampled. North arrow applies to all islands. Facies delineations were made by a neural network based on field surveys and satellite-derived digital elevation data (TanDEM-X from the German Aerospace Center) and our own field surveys. See Material and Methods in Dyer et al. (2021) for details.

uncertainty calculations see Dyer et al. (2021)). We determined a mean sea-level reference frame for the surveyed islands in order to relate data from the differential GPS to the tidal datum. We deployed tide gauges near study areas for several days to a week during field campaigns and determined the elevation of the measured mean water level on the ellipsoid reference frame of the differential GPS data (specifically, World Geodetic System 84 also known as WGS, 1984, EPSG:4326). To estimate the elevation and uncertainty of mean tide level around the archipelago, we used 2D Gaussian process regression to combine our short-term tidal data with a long-term tidal and elevation dataset from Settlement Point on Grand Bahama Island (Caldwell et al., 2015) and with the GM2008 (Earth Gravitational Model, 2008) geoid model (Dyer et al., 2021). We assign 10 cm uncertainty to this method of estimating mean sea level from a small set of tidal cycles. We adjusted the GPS measurements to this local mean sea level. Total elevation uncertainties were calculated by adding the uncertainty from each source in quadrature. The samples' elevations and their uncertainties are found in Table 1.

2.2. U-series chronology

The first step in interpreting sea-level history based on fossil corals is assessing their preservation and potential degree of diagenetic alteration. This assessment enables us to identify corals that are pristine, or nearly so, and thus are least likely to have lost or gained uranium or thorium since their deposition, therefore are more likely to display closed-system behavior. A detailed description of our rigorous protocol for sample screening, preparation, and analysis is also reported in Sandstrom (2021). We selected coral fragments of ~200 mg from the dense theca material (the skeletal wall), which is typically less affected by diagenesis and recrystallization than the commonly used bulk material (Obert et al., 2016). Prior to U-series analysis, these samples were carefully powdered and a ~20 mg aliquot from each coral was examined by X-ray diffraction to estimate the aragonite content. We then used a ^{229}Th–^{233}U–^{236}U triple spike calibrated to the Harwell uraninite (HU-1) standard reference material, assumed to be in secular equilibrium with respect to both ^{230}Th/^{238}U and ^{234}U/^{238}U. Samples were dissolved in HNO_3, followed by the isolation of U and Th from the solution through co-precipitation with $Fe(OH)_2$, redissolution, and column chemistry using Bio-Rad AG 1 × 8 200–400 mesh anion resin. Isotope ratios were measured on a ThermoScientific Neptune Plus Multi-collector ICP-MS at the Lamont Doherty Earth Observatory of Columbia University. For U analyses, we measured ^{233}U, ^{235}U, ^{236}U and ^{238}U in Faraday cups, and ^{234}U in a secondary electron multiplier (SEM) detector simultaneously, using an RPQ (Retarding Potential

Table 1
Overview of corals dated in this study including their location, habitat reef zone, species, and the mean and maximum (97.5%) values of their water depth.

Location	Site name	Sample	Longitude (DD)	Latitude (DD)	Type of reef	Reef zone	Genus dated	Sample elevation(m)		Water depth	
										mean	max
Crooked Island	Landrail Point	B808-1A	−74.340	22.803	Shelf-edge	rear	*Pseudodiploria* sp	1.09	0.05	2.0	5.3
		B808–1B	−74.340	22.803			*O. annularis*	1.47	0.04	2.0	5.3
		B808–1C	−74.341	22.803			*Pseudodiploria* sp	−0.07	0.05	2.0	5.3
	Major Keys Harbor	B806	−74.200	22.768	Dune	inshore	*Pseudodiploria* sp	−0.10	0.15	1.4	3.3
	McKay's Bluff	B809	−74.175	22.755	Dune	inshore	*O. annularis*	1.64	0.23	1.4	3.3
	McKay's Bluff headlands	B810-1A	−74.173	22.754	Lagoonal	lagoon	*O. annularis*	1.30	0.21	2.0	5.3
	Left Foot Headlands	B811-1A	−74.167	22.751	Dune	inshore	*Pseudodiploria* sp	1.62	0.16	1.4	3.3
	Half moon dune	B1118–C	−74.154	22.742	Dune	inshore	Diploria	1.67	0.22	1.4	3.3
	West T bone ridge	B1109–B	−74.132	22.739	Dune	inshore	*O. annularis*	−0.21	0.19	1.4	3.3
	T bone east	B1117–B	−74.112	22.737	Dune	inshore	*O. annularis*	1.43	0.20	1.4	3.3
	T bone east	B1116-E	−74.111	22.736	Dune	inshore	*Pseudodiploria* sp	0.70	0.20	1.4	3.3
	West Bullet Hill	B1108-A	−74.103	22.743	Dune	inshore	*Pseudodiploria* sp	1.02	0.22	1.4	3.3
Long Cay Long Island	Long Cay	B1112-D	−74.381	22.553	Shelf-edge	rear	*Pseudodiploria* sp	2.31	0.33	1.4	3.3
	Old Grey's	B1123–C1	−75.089	23.242	Shelf-edge	rear	*Pseudodiploria* sp	2.23	0.18	1.4	3.3
		B1123-Z1	−75.089	23.242				2.66	0.18	1.4	3.3
		B1123–Y1	−75.089	23.241				2.70	0.18	1.4	3.3
	South point	B1125-Z1	−74.853	22.857	Lagoonal	lagoon	*Pseudodiploria* sp	1.54	0.36	2.0	5.3
		B1128-Z	−75.045	23.082	Dune	inshore	*O. annularis*	1.88	0.16	1.4	3.3
	Middle-south point	B1129–Y1	−74.851	22.955	Lagoonal	lagoon	*Pseudodiploria* sp	2.16	0.35	2.0	5.3
		B1129–C	−74.851	22.952				2.42	0.35	2.0	5.3
		B1129-Z-O	−74.851	22.950				2.24	0.35	2.0	5.3
Eleuthera	Whale Point	BEL-WP-1C	−76.619	25.460	Lagoonal	lagoon	*Diploria*	4.87	0.30	2.0	5.3
		BEL-WP-1D	−76.619	25.460			*Pseudodiploria* sp	4.87	0.30	2.0	5.3

Quadrupole) high abundance sensitivity energy filter. For Th analyses we used a multi-dynamic routine, alternating ^{229}Th and ^{230}Th on the multiplier behind the RPQ filter, while measuring ^{235}U and ^{238}U (added in known amounts to the Th aliquots) on Faraday cups in order to monitor and correct for instrumental mass fractionation. A third scan checked the amount of ^{232}Th. To assess and correct the SEM-Faraday gain we used sample-standard bracketing. For U runs we used the CRM-145 U-standard, with ^{238}U and ^{235}U measured on Faraday cups and ^{234}U measured on the SEM. To correct for instrumental mass fractionation and bias we used the US Department of Energy certificate values of ^{235}U/^{238}U = 0.0072543 and ^{234}U/^{238}U = 0.000052841; their errors of 0.16% and 0.06%, respectively, are not propagated into the ages. For Th analyses, we used an in-house gravimetrically mixed Th standard from NIST SRMs 4342 and 4328 so that ^{229}Th/^{230}Th ~1. All the U and Th runs were corrected for instrumental mass fractionation by normalizing the measured ratio of ^{238}U/^{235}U to a value of 137.88 (the choice of a value has no impact on the final ages as long as it is the same for both U and Th analyses). All samples showed very low ^{232}Th signals, with typical ^{238}U/^{232}Th values in the range of 10^3 to 10^4, hence no tailing corrections on ^{230}Th were necessary, and initial ^{230}Th is negligible. Washout intensities between samples were monitored after each measurement to ensure no cross-contamination. Ages are reported relative to the year of analysis, 2020–2021, were calculated using the decay constants of Cheng et al. (2013) and do not include their uncertainties. Data detrending, reduction, age calculation, and uncertainty assessment were conducted off-line using a MS Excel spreadsheet. All measurements are reported with ±2σ absolute uncertainties and include combined propagated analytical uncertainties as well as systematic uncertainties calculated via replicate analysis of appropriate standard materials. The U and ^{232}Th concentrations, the isotope activity ratios, and coral ages from Crooked Island and Long Cay, Long Island, and Eleuthera are listed in Table S1.

We evaluated how closely the samples followed closed-system behavior using the following criteria:

(i) *Coral samples are primary aragonite (>98%).* Since the presence of calcite indicates diagenetic alteration and thus, U and/or Th exchange since the death of the coral, only samples with less than 2% calcite were further processed and analyzed.

(ii) *The uranium concentration falls within range of living corals of the same species.* Secondary addition or loss of U will bias results towards younger/older ages, respectively. We used the window of U concentration of 2.12–3.32 ppm for *O. annularis* and 2–3.2 ppm for *Pseudodiploria* sp specimens suggested by Scholz and Mangini (2007).

iii) *The ^{232}Th concentration is lower than* 3 ppb. This threshold value for the detrital Th contamination used by different laboratories is typically context-based. Some studies involving MIS 5e corals have used a threshold of 2 ppb for screening (Scholz and Mangini, 2007). However, this level of contamination mainly has an effect on younger corals (less than 5 ka (Cobb et al., 2003);), hence, we allowed for a threshold of 3 ppb.

iv) *$\delta^{234}U_i$ value within* −5‰ to +7‰ *of ~145‰ value for modern corals/seawater.* A common characteristic of MIS 5e U-series coral ages is a systematic open-system bias towards too high ^{234}U/^{238}U and ^{230}Th/^{238}U, resulting in closed-system ages that are too old.

In order to deal with this problem, many studies have only considered data where $\delta^{234}U_i$ is within ±5‰ of the average value for modern corals/seawater (~145‰; Chutcharavan et al., 2018), assuming that δ^{234}U of seawater remained nearly constant, which appears reasonable for interglacials over the last 400 kyr (Henderson and Anderson, 2003). An extension of 2‰ of the higher end of ±5‰ range has been recently suggested by Chutcharavan and Dutton (2021), despite the fact that it implies less pristine samples and allows for larger differences between the measured and true ages. This was done partly because the average δ^{234}U of seawater is not well constrained during MIS 5e and the subtle biases in interlaboratory calibration protocols could result in systematic offsets of a few per mil.

v) *Replicate subsamples of the same coral yield the same ages and activity ratios within their associated uncertainties.* To better estimate how well our data reflect the real age variability (Scholz and Mangini, 2007) and to examine the effects of diagenetic processes in more detail, we analyzed replicates (separate samplings of the same coral head) on eight of our samples.

Our rigorous screening protocol for identifying nearly pristine corals was successful in that all but 2 samples fell within the limits of −5‰ and +7‰ of $\delta^{234}U_i = 145‰$ suggested by Chutcharavan and Dutton (2021). However, the majority of our samples fall above $\delta^{234}U_i = 145‰$ (see Fig. 4 in the Results and Discussion section) which indicates a small amount of open-system behavior (impacting the calculated age on average by < 1 kyr). We find a trend between the closed-system ages and $\delta^{234}U_i$ for the majority of our samples (Fig. S1A) and show that it imparts a small systematic age bias caused by the open-system behavior (see Section ^{234}U–^{230}Th ages of fossil corals in the main text), since applying the model of Thompson et al. (2003) to correct our data for the open-system behavior eliminates the trend (Fig. S1B). For this reason, we favor the open-system corrected ages as reflecting better estimates of the true ages, but we present the results for both closed- and open-system ages. Although this model may not be globally applicable to calculate open-system ages (Stirling and Andersen, 2009), it is well-suited to correct diagenetic arrays common to the Caribbean and The Bahamas (Muhs et al., 2020; Skrivanek et al., 2018).

2.3. Bayesian inversion and GIA modeling

To infer MIS 5e GMSL from our local sea level observations, we apply the methodology described in Dyer et al. (2021) and summarized here. We first account for the indicative range of each coral using present-day observations of coral depth distributions (as described in Paleo-habitats of the surveyed coral reefs and their paleowater depth estimate in the Results and Discussion section). We combine this indicative range with each coral's U-series age, elevation, and location to produce sea-level index points. We then correct the elevation distributions for GIA and long-term subsidence using Gaussian process regression within a fully Bayesian framework.

For the GIA correction, we compare our new coral sea-level index points, along with previously published data on corals (Chen et al., 1991; Muhs et al., 2020; Thompson et al., 2011) and marine-limiting points from sediments across the Bahamian archipelago (which have been assigned an assumed age; Dyer et al., 2021), to a suite of GIA model predictions. We note that for the open-system ages we used the $^{230}Th/^{238}U$ and $^{234}U/^{238}U$ values recalculated by Chutcharavan and Dutton (2021). We use a 579 member GIA ensemble, which includes models produced with six different sizes and distributions of the former (MIS-6) North American ice sheet, two different timings for the onset of penultimate deglaciation, and 48 different viscosity structures of the Earth. We additionally include three runs that account for lateral variations in Earth's viscosity structure from Austermann et al. (2021). We calculate a weight for each GIA model based on how well the model captures the spatial trends in the data and calculate a combined GIA correction using these weights. We note that this correction accounts for GIA associated with ice volume changes prior to and after MIS 5e, but does not include GIA associated with ice volume changes during MIS 5e (which are relatively small in The Bahamas (cm to dm)), as detailed in Results and Discussion. Following McNeill (2005), we treat subsidence between MIS 5e and the present-day as uniform across the archipelago and model it as a normal distribution centered at 2.5 m at 125 ka with a 1-sigma of 0.5 m, which means that 98% of solutions are between 1.5 and 3.5 m. We then use Bayesian inference to infer GMSL by combining the composite GIA correction with prior knowledge about the corals' elevations, water depths, and the long-term Bahamian subsidence rate. Temporal interpolation is done using Gaussian process regression. We acknowledge that if there is variation in subsidence across The Bahamas, it may affect our GMSL inference significantly since the GIA model weighting assumes that any spatial variability is driven by GIA alone. This approach allows us to incorporate data with different age uncertainties and indicative water depth ranges to estimate how GMSL (and its uncertainty) changes over time.

2.4. Fingerprint analysis

AIS and GrIS melt and regrowth during MIS 5e caused RSL to vary in space and time as the shifting ice masses perturbed Earth's gravitational field, deformed its surface, and altered its rotational state (Hay et al., 2014). We model six melt scenarios for the GrIS (two scenarios are presented in the Results and Discussion section and the other four are in the Supplemental material) and investigate how much RSL in The Bahamas deviates from the ice equivalent global mean. Most GrIS models for MIS 5e indicate peak melt between 125 and 120 ka, slightly lagging the northern hemisphere summer insolation maximum, with magnitudes of peak melt varying from 0 to 5.5 m ice equivalent GMSL above present (Calov et al., 2015; Goelzer et al., 2016; Plach et al., 2019; Quiquet et al., 2013; Yau et al., 2016). For our study we choose the high and the low GrIS melt scenario from Calov et al. (2015). We then model the response of Bahamian sea level using a gravitationally self-consistent GIA model that accounts for shoreline migration and feedbacks into Earth's rotation axis (Kendall et al., 2005). In the GIA calculation we assume that the Earth's elastic structure follows PREM (Dziewonski and Anderson, 1981) and vary three parameters of the viscous structure: an elastic lithospheric thickness that is either 71 km or 96 km, an upper mantle viscosity that ranges from 0.3 to 0.5 × 10^{21} Pa s, and a lower mantle viscosity that ranges from 3 to 40 × 10^{21} Pa s. We average the resulting RSL response across all locations that have coral data and all viscosity structures to obtain a mean and standard deviation for local sea-level response. In a second step we subtract this local sea level from the inferred GMSL (calculated in Fig. 6). The results are sea-level changes in The Bahamas driven by water sources other than the GrIS, such as mountain glaciers, thermal expansion, and the Antarctic ice sheet, with the latter likely driving the majority of this signal. In summary, this final step helps us partition MIS 5e GMSL into melt contributions from the GrIS and AIS, and assess the timing of these contributions.

3. Results and Discussion

3.1. Paleo-habitats of the surveyed coral reefs and their paleowater depth estimate

Fossil corals are found around most Bahamian islands, but previous chronological studies of reef development during MIS 5e have been dominated by work on the west coasts of New Providence (Muhs et al., 2020), San Salvador, Great Inagua (Chen et al., 1991; Thompson et al., 2011), and West Caicos (Kerans et al., 2019). We observed MIS 5e fossil coral reefs outcropping between 0 and 4.4 m above present sea level along the coastlines of Crooked Island, Long Cay, Long Island, and Eleuthera (Fig. 1) and present new data on corals mainly from their north and east coasts (Fig. 1C, D, E). The dominant coral species include *Orbicella annularis*, formerly known as *Montastraea annularis*; *Pseudodiploria* sp., previously known as *Diploria; Acropora palmata*; *Acropora cervicornis;* and *Porites porites*. Some of these corals can grow at significant depths (Chutcharavan and Dutton, 2021; Hibbert et al., 2016; Muhs et al., 2020; Skrivanek et al., 2018), hence considering the full depth range of each taxon separately leads to a very large range (and therefore large uncertainty) of paleo sea level.

To better estimate paleo water depths of individual corals, we carefully established the paleo habitat of each reef. Based on our field observations, we determined that the MIS 5e corals we sampled would have either formed in the shelf-edge coral framework or grown in the lagoon. The latter forms in patch reefs or as isolated corals growing on the submerged flanks of lithified dunes; these corals are typically characterized by low spreading growth forms that usually adhere to rocky surfaces. The different coral reef environments are shown in Fig. S2 and described below. Corals in growth position (found in the correct growth orientation and with a clear basal attachment to the reef substrate at the outcrop scale) have been recognized in each of these environments, both

in MIS 5e deposits and in modern reef systems. Although not perfect representations of MIS 5e coral habitats, modern reefs provide an analogue close enough to enable us to develop conceptual understandings and predictive models. The combination of stratigraphic context and water-depth ranges of present-day reef assemblages produces strong justification for our tighter paleo water-depth estimates. Our approach relies on coral water depth observations associated with the structural zones reported by Goreau and Goreau (1973) and Skrivanek et al. (2018). We model the water depth of each coral using an inverse Gaussian distribution defined by mean (μ) and shape (λ) parameters (Fig. 2), where the maximum values are equal to the 95th percentile of the distribution. The mean and maximum values are reported below and summarized in Table 1.

a) *Shelf-edge coral framework* – although commonly referred to as barrier reefs or reef crests, we retain the nomenclature proposed by Khaled bin Sultan Living Oceans Foundation in their world's largest Global Reef Expedition (Carlton et al., 2021). These coral reefs grow near sea level on the platform edge, parallel to the shore but separated from it by a channel of deep water, in a setting where water moves primarily through tides and wind driven currents. We interpret these reefs as the most seaward coral deposits from MIS 5e that still exist today. Corals that thrive in this zone are in general more complex reefs and have structures strong enough to endure intense wave action, high light intensity, and subaerial exposure. We identified three outcrops preserving examples of these reefs: Land Rail Point on Crooked Island, Long Reef on Long Island, and a reef on Long Cay (Fig. 1). These sites are all characterized by extensive coral colonies, massive coral heads, high species diversity, and high coral density. They are typically observed in a shallowing-upward parasequence of facies, where the fossil coral reefs occur as the lowermost sediments, often co-existing with burrow-filled carbonate sands and muds with marine fossils, overlain by cross-stratified coarser carbonate sands. We assigned shelf-edge corals a mean and maximum paleo water depth of 1.4 and 5.3 m, respectively (see Table 1), except for corals at the Landrail Point site, where we chose a more conservative mean water depth estimate of 2 m in the absence of a red coralline algae crust.

b) *Lagoonal corals,* also known as back reef corals, make up patch reefs of diverse sizes and shapes. The modern Bahamian lagoon is only a few meters deep at maximum and due to its calm and stable environment, it represents an ideal and extensive habitat for coral reefs. These habitats tend to occur at sites with a well-developed shelf-edge coral framework, which protects the area and contributes to the development of a low-energy, restricted environment. Corals thrive

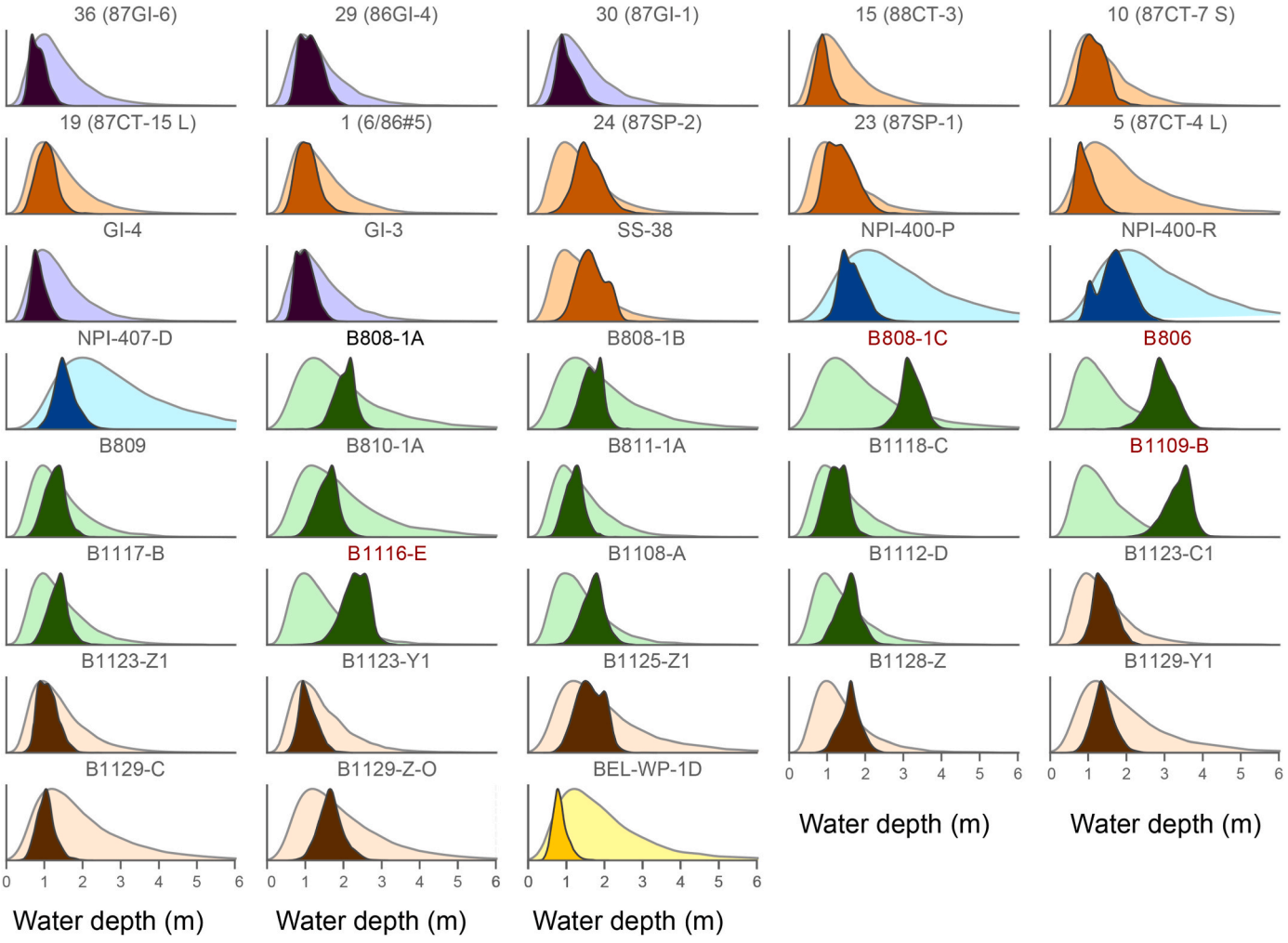

Fig. 2. The prior (light shade) and posterior (dark shade) distributions for paleowater depth estimates corresponding to each coral used in our inversion. Posterior depth estimates are obtained using open-system corrected U-series ages. Note that this plot includes both the newly dated corals as well as those previously published by Chen et al. (1991), Muhs et al. (2020), Thompson et al. (2011). Corals are color coded by island: Great Inagua (purple), San Salvador (orange), New Providence Island (blue), Crooked Island and Long Cay (green), Long Island (brown), and Eleuthera (yellow). Y axis shows the probability density. The bold red labels mark the corals for which the inversion suggest that they formed at slightly deeper depths than the prior suggests.

where there is little sedimentation. The shallow water depth and accumulation of muddy sediments in lagoonal areas therefore restrict the spatial extent of corals, resulting in their patchy occurrence. These reefs can be as small as a few meters in diameter and corals occur individually or in clusters. We identified lagoonal reefs at sites B810-1A, B1125, and B1129 (Table 1) on Crooked Island, where large but isolated heads of *O. annularis* are dominant. We also identified corals that grew on top of flooded lithified aeolian dunes as isolated corals. We interpret their formation as a time-transgressive process: in early MIS 5e (or possibly even earlier, i.e., MIS 7, 9, 11) dune systems formed on land (the lithification process happens rapidly; Halley and Harris, 1979) and, as GIA drove sea-level rise throughout the interglacial, these dunes were submerged. This process is evident in the Holocene throughout The Bahamas, where radiocarbon dated dunes of the North Point Member of the Rice Bay formation have foresets that dip into the ocean (Hearty et al., 2007); we observed that these foresets are often colonized by encrusting *Pseudodiploria* sp.. These corals are similar to ones described by (Hearty et al., 2007) in their stratigraphic sketches of Rocky Dundas in the north-central Exumas and Hole in the Wall on Great Abaco Island. On the topographic map (Fig. 1), the older MIS 5e fossil dunes where we identified this type of coral habitat are seaward of the dunes on the modern beaches. These corals are widespread, especially at sites along the northeast-facing side of Crooked Island (Table 1, samples labeled 'Dune'). They exhibit low species diversity (most commonly *Pseudodiploria* sp. and *O. annularis*). We assigned these corals a maximum paleo water depth of 5.3 m (mean of 2 m) for patch reefs and 3.3 m (mean of 1.4 m) for dune corals (see Table 1)

The water depths described above and shown in pastel colors in Fig. 2 constitute our prior knowledge of each coral's water depth. We determined the most likely water depths for each coral by combining their elevation and chronology, the changes in the relative sea level across space and time from GIA, and the range of possible time-varying GMSL histories. Using prior estimates on these quantities along with the simple relationship that local sea level is the combination of GIA, GMSL, and long-term subsidence, we calculate posterior estimates for each quantity including the inferred coral water depth. From these estimates, then we can explicitly state the water depths of each individual coral. For example, we infer coral B1123–C1 at Old Grey's site in Long Island to have lived at ~3 m water depth. There are two ways that corals of the same age can have different elevations on different islands: 1) GIA differences between the islands have offset the corals or 2) the corals grew in different water depths. We note that our model considers the full range of water depths for each coral independently, which is a more conservative approach than in some previous studies (Muhs et al., 2020; Skrivanek et al., 2018). When the posterior distribution for a modeled value is narrower than the prior distribution, the inference has taught us something, in that we know more than we did prior to the calculations. Most of our coral samples have posteriors near the mean of the prior, which indicates that our initial assumption about the mean was appropriate but the maximum water depth may have been too conservative (e.g., too deep). Samples B808–1C (shelf-edge), B806, B1109–B, and B1116-E (dune corals) from Crooked Island are the exceptions for which the inversions suggest they formed at deeper depths than the prior mean. These four corals are presently found at a lower elevation than corals of similar age from the same and neighboring sites; their prior paleo water depth should therefore be slightly deeper.

3.2. ^{234}U–^{230}Th ages of fossil corals

Selecting data using preservation threshold criteria. In order to assess the reliability of our U-series ages, we evaluated how well our samples exhibited closed-system behavior by considering mineralogy, U concentration, ^{232}Th content, the initial $^{234}U/^{238}U$ ($\delta^{234}U_i$), and how well the ages are replicated, as described in the Methods section. A step-by-step application of our screening criteria is shown in Fig. 3.

First, we apply a threshold of 3.32 ppm for *O. annularis* and 3.2 ppm for *Pseudodiploria* sp specimens (as suggested by Scholz and Mangini (2007)) for U concentration by comparing our values in the fossil corals to the modern analogues of the same species. This criterion allows us to identify addition or loss of uranium since the time of formation. We recognize that the data on modern corals is limited (Hibbert et al., 2016), therefore, we did not exclude two samples that have slightly higher U concentrations from our evaluation (B809-1A and B1108–O-A that have U concentrations of 3.48 ppm and 3.42 ppm, respectively) (blue circles Fig. 3A). Then, we apply a threshold for ^{232}Th concentration: there are three samples that have ^{232}Th higher than the threshold of 3 ppb: B808–1C, B1108–B-M, and B1119-A-M, with the last two having substantially higher ^{232}Th concentrations (Fig. 3A). These samples are excluded from our discussion and are listed separately from the rest of the data in Table S3.

Next, we consider the $\delta^{234}U_i$. One of the issues with U-series dating of MIS 5e corals is that the vast majority of measured samples have variable $\delta^{234}U_i$ values that deviate from modern seawater, indicating open-system U-series behavior since the time of coral growth with most toward higher values. In The Bahamas, this is clearly shown by the $\delta^{234}U_i$ values of a compilation of published data (Fig. 4, grey symbols). However, in our suite of samples (Fig. 3, green symbols), all but two fall within the narrow $\delta^{234}U_i$ range of 143.8–151.3‰, and thus are within the −5‰ to +7‰ window of the present-day $\delta^{234}U$ value of 145 used to filter out the "reliable" closed-system ages, as suggested by Chutcharavan and Dutton (2021) (Fig. 3B and 4).

We attribute the tight clustering of our data near modern seawater $\delta^{234}U_i$ values to our rigorous sample preparation protocol. The exceptions are the same two samples that had high ^{232}Th concentrations, B1108–B-M and B1119-A-M; these are not discussed further. Regarding the age variability, all replicated samples yielded ages that overlap or nearly overlap within analytical uncertainty between different subsamples from the same coral for both closed-system ages (Fig. 3C) and open-system ages (Fig. 3E). This overlap indicates negligible within-sample variability and that the analyses adequately describe each sample, confirming the near closed system behavior. For these replicate samples we calculated and compared the arithmetic mean and the weighted mean. The results overlap within their uncertainties and we chose to use, in the further analysis, the arithmetic mean of their isotope ratios with propagated uncertainties. Finally, a summary of which samples passed/failed the criteria is shown in Fig. 3D and F, where the two high Th samples "failed", three are considered "reliable", and the rest are "most reliable". We note that the species that were the best preserved and passed our threshold criteria are *Pseudodiploria* sp. or *Orbicella annularis*, the same specimens that were found in growth position in the units described by Skrivanek et al. (2018).

Correcting for open-system behavior. As already noted, a common characteristic of MIS 5e U-series coral ages is a systematic open-system bias towards too high $^{234}U/^{238}U$ and $^{230}Th/^{238}U$, yielding erroneously old closed-system ages (shown by most of the literature published data for Bahamian corals, plotted in grey markers in Fig. 4). To overcome this problem, it is often assumed that ages of samples that fall close to the evolution pathway of modern seawater (dark blue line in Fig. 4) are likely not biased much by open-system behavior. Nevertheless, Thompson et al. (2003) showed that samples that deviate significantly beyond that reliability range, i.e., much more than our samples, can be corrected using their open-system correction model. Although all but two of our samples fall within the strict "reliability" range, most of the data are above the seawater evolution line (Fig. 3B and 4). Assuming a paleo seawater $\delta^{234}U_i$ of 145‰, suggests that most samples therefore, show a small amount (averaging <1 kyr) of open system behavior that indicates that their true age is slightly younger than the calculated closed-system age. We acknowledge that the open-system correction would be slightly different if the $\delta^{234}U_{sw}$ value was different; for example, if $\delta^{234}U_{sw}$ was 147‰ it would shift the samples towards

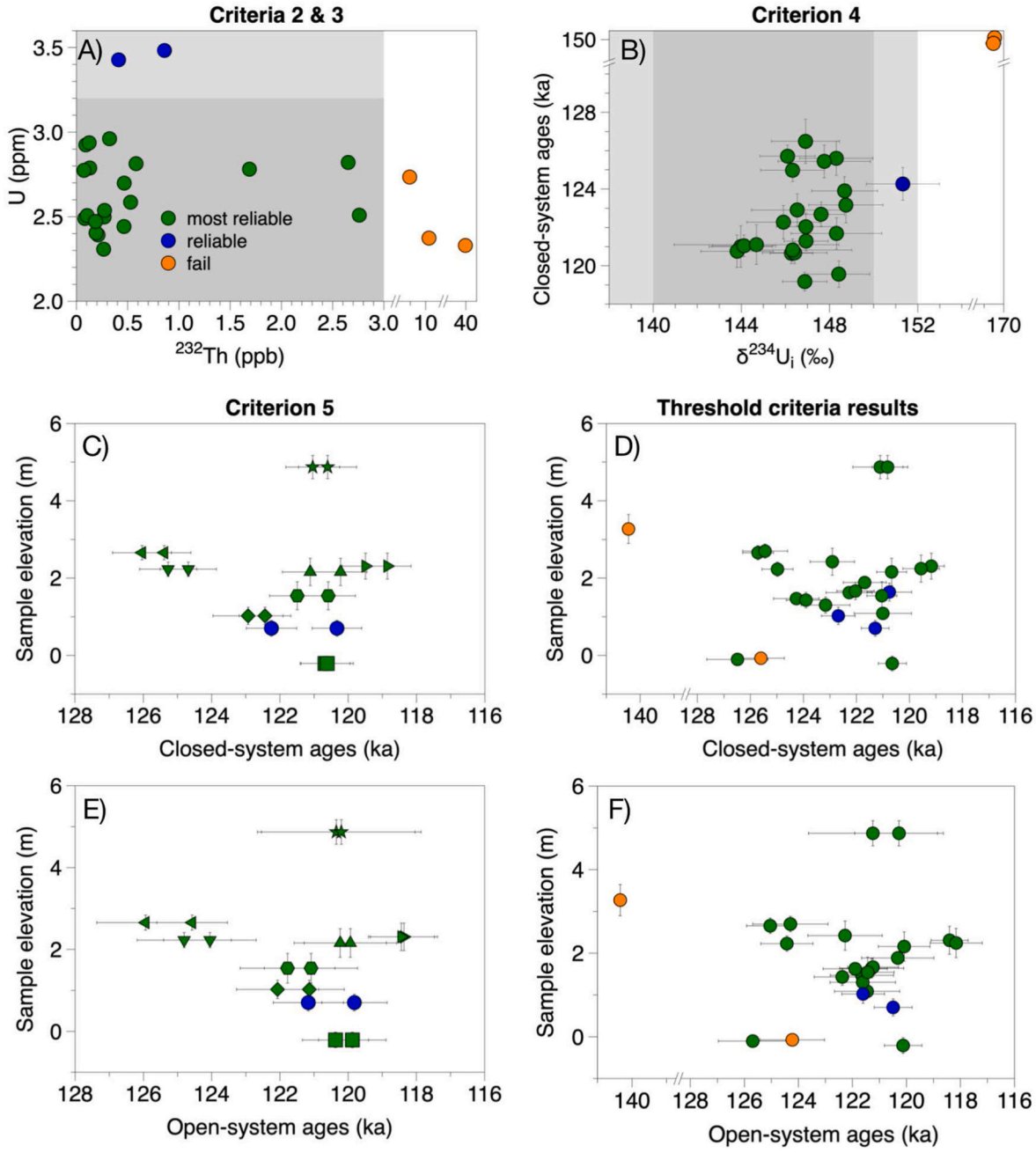

Fig. 3. Step-by-step application of screening criteria: A) U concentration (ppm) within the range of modern analogues from the same species vs ^{232}Th content (ppb) (Criteria 2 and 3); B) $\delta^{234}U_i$ vs closed-system age (Criterion 4). In panel A) and B) the dark shaded grey area represents the interval that we consider "most reliable," and light shaded grey area, the interval considered "reliable"; C) and E) individual closed and open-system ages, respectively, of eight replicated samples marked by different symbols (Criterion 5); D) and F) the data that passed/failed all the criteria for closed and open-system ages, respectively. If data passed one criterion but failed another they are considered to have failed overall. In all panels green/blue/orange points represent samples that are most reliable/reliable/fail the threshold criteria, respectively. Age uncertainties are 2σ and elevation uncertainties are 1σ.

slightly older ages, but this shift is small (averaging ~ 0.8 ka), which is within the ages' uncertainties.

In our data we find a trend between the closed-system ages and $\delta^{234}U_i$ for the majority of our samples (dark blue circles in Fig. S1) that shows older ages with higher $\delta^{234}U_i$. To test whether this trend is indicative of a systematic open-system effect on our U-series data, we calculated the open-system ages of our corals using the Thompson et al. (2003) model (Fig. S2B), which shifts the majority of samples towards slightly younger ages and impacts the age distribution (Fig. S1). The open-system corrected ages show no trend with $\delta^{234}U_i$, which indicates that the open-system behavior of our samples caused a small (average ~0.8 ka) but systematic age bias on the closed-system ages. Applying the open-system correction thus improved the accuracy of coral age determinations by effectively eliminating apparent small but systematic errors in the closed-system ages. We therefore consider the open-system ages a better representation of the true ages. Nevertheless, in our data interpretation we explore the results obtained using both the closed- and open-system ages and discuss how the correction for open-system behavior impacts our posterior GMSL curve. All U-series results, their associated uncertainties, and both closed- and open-system ages are listed in Table S1 and shown in Fig. S1.

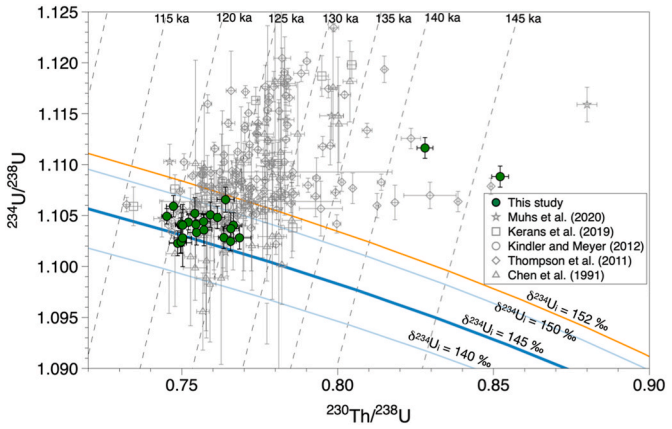

Fig. 4. U–Th isotopic evolution diagram for corals from Crooked Island and Long Cay, Long Island, and Eleuthera in comparison with previously published data from other islands from The Bahamas (recalculated by Chutcharavan and Dutton (2021)). Straight dashed lines are closed-system isochrons labeled in ka at their upper ends. The thick blue curve shows closed-system seawater evolution for $\delta^{234}U_i = 145‰$, the value of present-day seawater; the light blue curves mark the range of ±5‰ of 145‰ corresponding to the data window often considered close enough to closed-system evolution to be a reliable age; and the orange curve marks the +2‰ extension of the upper end (Chutcharavan and Dutton, 2021). All but 2 of the measured samples are within this range. Most of the data show slightly elevated $\delta^{234}U_i$ compared with present-day seawater.

3.3. Predictions of MIS 5e relative sea level (RSL) in the Bahamas

Following the approach of Dyer et al. (2021) we used Gaussian process regression in a Bayesian framework to infer the most likely GIA signal (from a set of 579 simulations including three 3D models) and GMSL history given the coral ages, elevations, and paleo water depths (see Materials and Methods). This approach also accounts for long-term subsidence of the archipelago. We combined the inferred GIA signal, GMSL history, and subsidence to obtain site-specific RSL that best fits the observations (the weighted average of the posterior RSL) for different Bahamian islands (Fig. 5). Given that the data were used to constrain the model, we expect a good data–model fit. We performed this analysis using both closed- and open-system ages of corals from other islands (Chen et al., 1991; Muhs et al., 2020; Thompson et al., 2011) included in Dyer et al. (2021), as well as those from our new samples. We show in Fig. 5 that the predicted sea-level evolution is very similar between the two sets of results, with slightly smaller uncertainty envelopes when using the open-system ages.

Our model predictions using the new corals' elevations and ages indicate a rising RSL early in the interglacial (128-124 ka) followed by a stillstand or minor sea-level fall (124-120 ka) and a final sea-level rise towards the end of the interglacial. We acknowledge that large truncation surfaces were observed in San Salvador and reported by Skrivanek et al. (2018); however, we do not see a systematic separation of our ages and elevations that would require a local sea level oscillation during MIS 5e. Nevertheless, this sea-level evolution allows, within uncertainty, a minor MIS 5e oscillation in local sea level at each island analyzed here (Fig. 5). We note that none of our coral sampling locations show geologic or stratigraphic indications of exposure or significant non-deposition/erosion indicative of a local sea-level oscillation; nonetheless, we acknowledge that corals are best suited for recording prolonged highstands rather than rapid GMSL fluctuations, being unable to catch up with rapid sea-level changes.

Our RSL reconstruction therefore does not preclude the possibility of a sea-level oscillation during MIS 5e, as previously proposed based on field observations of an erosional surface on Great Inagua and West Caicos (Kerans et al., 2019). This laterally discontinuous marine-erosion surface separates two MIS 5e reef units and was interpreted as an early sea-level rise represented by a reef-dominated unit across the region, followed by a short-lived sea-level fall, and capped by late MIS 5e rise (Chen et al., 1991; Thompson et al., 2011). We do not find evidence of four sea-level peaks as interpreted by Thompson et al. (2011), who reported U-series ages of corals sampled at sites previously investigated by Chen et al. (1991) from Great Inagua and San Salvador islands. Instead, our predicted sea-level history is more consistent with evidence of a minor sea-level lowering of ~1 m over a time period of ~1000 years, similar to that proposed by Skrivanek et al. (2018), rather than the larger drop in sea level of approximately 2 m (or possibly more) across this region as suggested by Dutton and Kerans (2021).

Muhs et al. (2020) reported detailed elevation measurements combined with high-precision U-series dating of patch reefs and beach ridges from New Providence Island and found that RSL was at least ~5–~7 m and ~5–~14 m higher than present, respectively. They further used their sea-level reconstruction to test the hypothesized GIA-model-derived RSL predicted by Creveling et al. (2015) under two scenarios with equivalent eustatic values of either +6 m (scenario #1) or +8 m (scenario #2), timed to occur at either the beginning (127 ka) or the end (120 ka) of MIS 5e. Creveling et al. (2015) modeled sea level in The Bahamas to be at 4 m (collapse scenario #1) or 6 m (collapse scenario #2) at the beginning of the MIS 5e, and under both scenarios, found higher sea level at the end of the MIS 5e than the beginning (9.5 m under scenario #1 and 11.5 m under scenario #2). Muhs et al. (2020) found that their field elevations from New Providence Island show generally good agreement with the GIA model estimates under either collapse scenario, if unadjusted for subsidence. Yet, our predicted RSL in New Providence Island (similar to Dyer et al. (2021); their Fig. 5), is on the lower end of the estimate from Muhs et al. (2020). We note that our GIA prediction is different due to the different ice history used. Our model, which chooses the ice history that produces the spatial RSL gradient that we observe across The Bahamas, finds that only models with MIS-6 Laurentide ice sheets that are smaller than the Last Glacial Maximum Laurentide ice sheet can explain the observed gradient. Our model preferred ice histories with these smaller MIS-6 Laurentide ice sheets produces a different RSL gradient across The Bahamas than the one found by Creveling et al. (2015) who assumed a penultimate glacial maximum ice history identical to the Last Glacial Maximum. We also point out that due to GIA, it is expected that RSL varies across the islands of The Bahamas, with the predicted magnitude of GIA being greater in the northern islands than in the southern ones (Fig. 1A and B). Hence, our RSL estimates from Crooked and Long Island (where the majority of our samples were collected) are expected to be lower than those from islands located farther north.

3.4. Global mean sea level estimates during MIS 5e

The Bayesian inference, which includes our new coral sea-level index points, the previously published data from corals (Chen et al., 1991; Muhs et al., 2020; Thompson et al., 2011; listed in Table S2), and the marine-limiting points from sediments across the Bahamian archipelago (Dyer et al., 2021), returns a most likely GMSL history, which can be calculated using U-series closed-system (Fig. 6A) or open-system (Fig. 6B) corrected ages. We highlight here that the GIA predictions used in our inference do not include any deformational, gravitational, or rotational effects associated with Greenland or Antarctic ice melt during MIS 5e beyond their present-day ice configuration. However, these effects are relatively small, as shown in the next section. While the spatio-temporal distribution of sea-level data is used to constrain the GIA contribution, this does not constrain or limit the GMSL inference, as shown by a synthetic test in Dyer et al. (2021). More details on the methodology are found in the Material and Methods section of Dyer et al. (2021). The results for the most likely GMSL curve are very similar when using the closed- and the open-system ages and show a GMSL of about 1 m throughout the entire course of MIS 5e. We find that GMSL

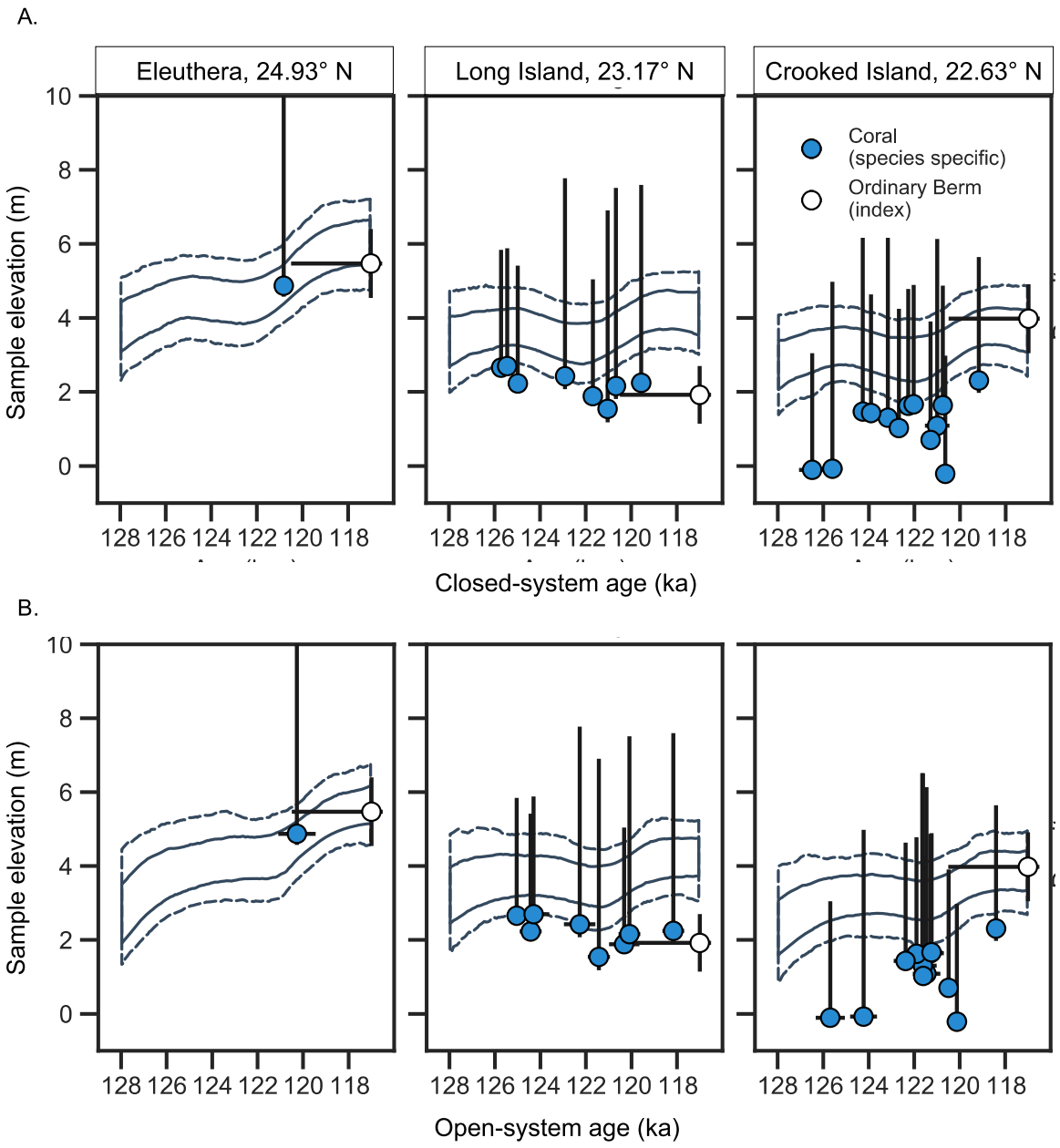

Fig. 5. Inferred site-specific RSL in Eleuthera, Long Island, Crooked Island and Long Cay (for the location of the islands see the white squares on Fig. 1A) with dark grey area representing the 68% envelope, and lighter grey are representing the 95% envelope. Since Long Cay is located near Crooked Island, the sample from Long Cay is included in the panels for Crooked Island. A and B show RSL using closed-system and open-system ages, respectively. Blue filled circles indicate the corals' present-day elevation and the black vertical line is the posterior coral water depth. White filled circles mark the outcrop observations of the boundary between aeolian sand and underlying beach facies plotted at the observed elevation offset downward by estimates of the elevation of the landward swash limit of constructive waves (the ordinary berms). We note that the berms have not been dated and have been assigned an assumed age and their paleoelevations were estimated using models of site-specific modern day wave run-up and mean high higher water (Lorscheid and Rovere, 2019).

likely exceeded 0.4 m (95% probability), but very unlikely (5% probability) exceeded 2.7 m using the open-system ages. However, when using the closed-system ages, this range increases from 0.4 to 5.3 m due to a bimodal distribution in possible solutions (Fig. 6A). We note that all these results include the second mode. It appears that the closed-system's slightly older ages force the inference scheme to upweight GIA models that allow for RSL in the Bahamas to peak earlier in the interglacial. The GIA simulations are particularly sensitive to older corals in MIS 5e because GIA correction in this region is greater early in MIS 5e than late. Biases in our inversion can be introduced if the GIA model suite does not capture the true deformational behavior of the region, or if the long-term subsidence estimate is incorrect or introduces spatial patterns that affect the GIA model inference.

Our new results indicate a GMSL lower than in Dyer et al. (2021), which found it very likely (95% probability) that global sea level peaked >1.2 m higher than today, and very unlikely (5% probability) that it exceeded 5.3 m. Here we show that including our new coral chronologies in the inversion and applying the open-system correction to all MIS 5e coral data across The Bahamas likely further narrows the range of compatible GIA models, which produced a slightly lower GMSL estimate. Additionally, our new coral elevations themselves, which are lower than the mean coral elevations used in Dyer et al. (2021), likely caused a lower GMSL curve. Our posterior GMSL curve, with most likely (68% probability) sea level between 1.1 and 2 m using closed-system

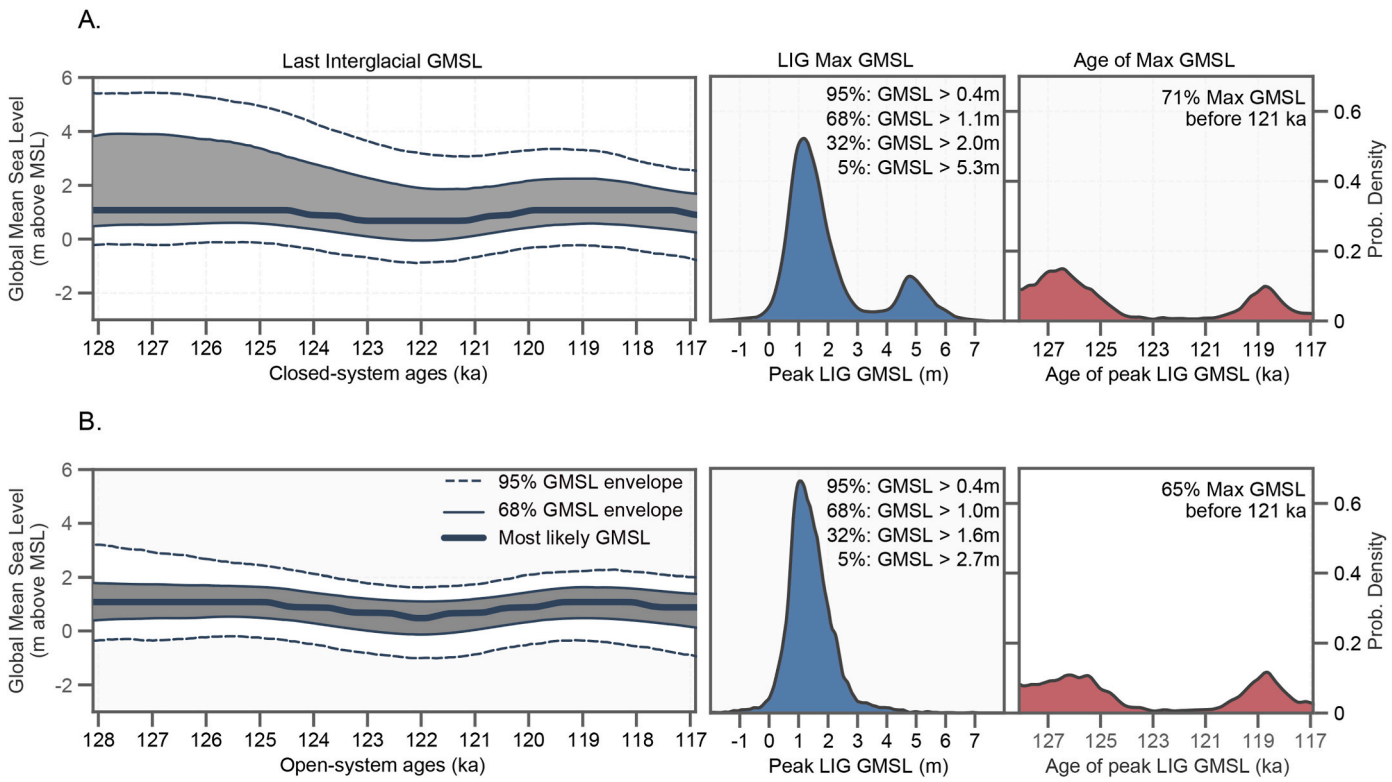

Fig. 6. Inferred MIS 5e GMSL estimates using: A) closed-system corrected ages and B) open-system ages. In the left panels, 68% of the solutions fall within the darker envelope and 95% of solutions fall within the lighter envelope of the most likely GMSL curve.

ages, and between 1 and 1.6 m using open-system ages, is notably lower than the previous estimates of 5–10 m above present sea level throughout MIS 5e including the range cited in the IPCC report (Fox-Kemper et al., 2021).

This begs the question whether our inferred GMSL is reconcilable with sea level observations elsewhere. To answer this question, we used our GIA model suite to calculate sea level at three locations with key sea level observations (Seychelles, Western Australia, and the Yucatan Peninsula). We used all Earth structures and all ice models except the ones with the largest and smallest Laurentide ice sheet, which have been shown to mostly not fit the data in the Bahamas. Each simulation (with varying ice and Earth model) was given equal weight and summed with

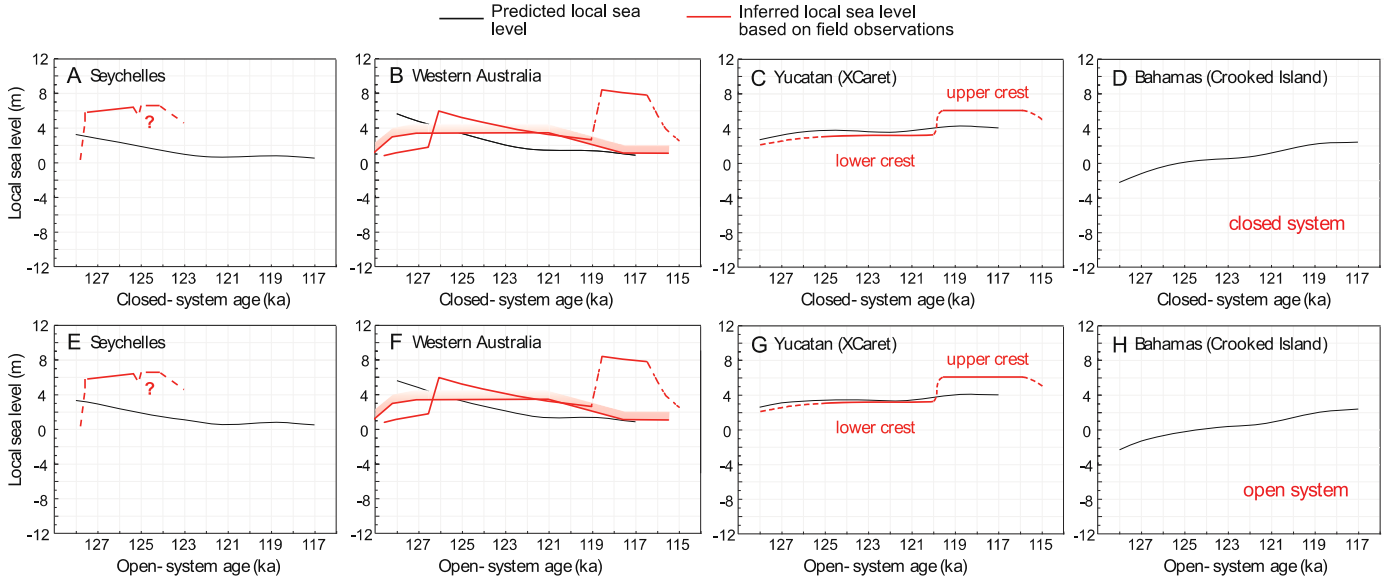

Fig. 7. A-D) Local sea level at the Seychelles (La Digue), Western Australia (Cape Range), Yucatan Peninsula (Xcaret), and The Bahamas (Crooked Island, Long Key), respectively. Red lines show the inferred local sea level at each site based on a variety of observations, with shaded regions marking uncertainties cited in the original publications: Seychelles (Dutton et al., 2015); Western Australia, line without uncertainty (O'Leary et al., 2013) and line with uncertainty (Dutton and Lambeck, 2012); Yucatan (Blanchon et al., 2009); Bahamas, with 68% and 95% uncertainty envelopes (this study). Black line with envelope is the predicted local sea level, which comes from summing GIA, GMSL, and in the case for The Bahamas, longterm subsidence. Shading indicates 68% and 95% uncertainty envelopes and line is the 50th percentile predictions.

the inferred GMSL (Fig. 6). Local sea level was calculated this way for both our closed-system (Fig. 7A–D) and open-system (Fig. 7E–H) results for GMSL. We find that observations in the Seychelles (Dutton et al., 2015) infer sea level that is compatible with our closed-system age results but are slightly above our open-system age results for local sea level (Fig. 7A, E). Observations from Cape Range in Western Australia (Dutton and Lambeck, 2012) are consistent with both scenarios, however a putative late peak in sea level as proposed by O'Leary et al. (2013) is inconsistent (Fig. 7B, F). Observations from XCaret on the Yucatan Peninsula fall within our range of predicted local sea level, however, our predictions do not require a specific step up in sea level as suggested by Blanchon et al. (2009) (Fig. 7C, G). Repeating this exercise for Long Island shows how large the range in GIA model predictions is when each model is weighted equally (grey bands) compared to models being weighted to fit spatial gradients in the sea level field (red bands, which equal results shown in Fig. 5). We note that locations other than The Bahamas are not corrected for possible longterm deformation and that the GIA correction will be affected by the fingerprint of the excess melt source (Hay et al., 2014), which is not considered here. To further scrutinize our results and to refine estimates of MIS 5e GMSL, we would need to jointly invert for reliable sea level (paleo water depth and ages) from multiple locations, expand the GIA modeling suite, and account for the spatially varying fingerprint signal of the Antarctic and Greenland ice melt.

GMSL lower than the likely range cited in the most recent IPCC report (Fox-Kemper et al., 2021) was also inferred from a highly resolved record based on phreatic overgrowths on speleothems from Mallorca, Spain (Polyak et al., 2018). Those authors used nine GIA models to correct their relative sea-level record. Reducing this to one GIA model results in a GMSL that peaked at 5 m higher than today at ~127 ka, gradually fell and stabilized by 122 ka (as low as 2 m; their Fig. 4) and remained stable until the highstand termination at 116 ka. A comparison with our record is challenging because their result is very sensitive to the GIA model used and does not correct for deformation related to tectonics or dynamic topography, which can cause long term uplift or subsidence. Clark et al. (2020) also argue for MIS 5e GMSL lower than 5–10 m based on ice–ocean–atmosphere modeling. They indicate a GrIS and AIS retreat to their present extent at ~128 ka, with the majority of the GMSL rise occurring during Termination II (T II, MIS-6 to MIS 5e transition, about 136-129 ka). GMSL rise proceeded slowly between 128 and 126.5 ka, then accelerated until ~124 ka as ocean forcing drove the West Antarctic Ice Sheet's Amundsen Sea sector to collapse. These authors suggest that GMSL reached ~3.5 m by 124 ka and remained relatively stable at this position throughout the interglacial. This modeled GMSL evolution differs from our coral-based estimate at the beginning of MIS 5e, but accords with the stable GMSL that we

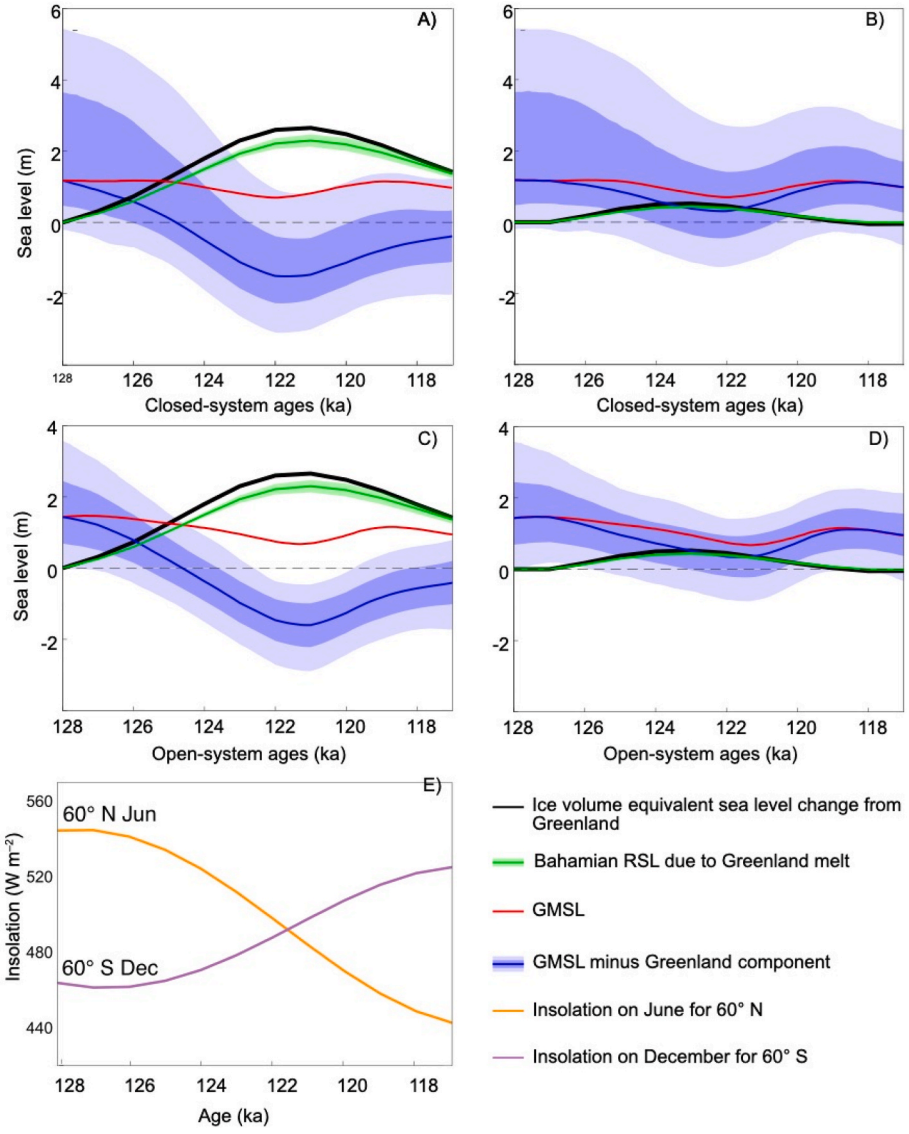

Fig. 8. Ice volume equivalent sea-level change for GrIS melt using two melt scenarios from Calov et al. (2015), black curves. A and B show results using closed-system ages; C and D using open-system ages for the median GMSL (red line). Resulting relative sea-level change in The Bahamas (green curve, mean and 1 standard deviation). Note that we omit uncertainties here for clarity; uncertainty bands can be seen in Fig. 6A. The non-Greenland component that drives sea-level change in The Bahamas is in blue (solid line is median, shading is 68% and 95% percentile envelope). E) Summer insolation curves for northern and southern hemispheres (Berger and Loutre, 1991).

infer between 124 and 116 ka, with no evidence of a significant late rise.

3.5. Implications for the source of MIS 5e sea-level highstand

In this final step, we use our new GMSL estimate to investigate the timing and possible sources of meltwater contributions to MIS 5e sea level. Ice loss produces a distinct geometry or 'fingerprint' of sea-level change for each ice sheet (GrIS or AIS (Hay et al., 2014)). For the GrIS sea-level contribution we consider the highest and lowest modeled melt scenarios from Calov et al. (2015), which span the entire range of other suggested models, such as those of Quiquet et al. (2013), Goelzer et al. (2016), and Bradley et al. (2018) (Fig. S3). Calov et al. (2015) used constraints of present-day surface mass balance partition and the surface elevation drop during MIS 5e compared to present at a position about 200 km upstream of the NEEM (North Greenland Eemian Ice Drilling) ice core site. In both scenarios melting starts ramping up at ~127 ka, attaining maximum ice loss at ~122 ka before the ice sheet gains mass again (Calov et al., 2015). The two scenarios vary in GrIS melt magnitude between ~3 m (black curve, Fig. 8A) and ~0.7 m GMSL-equivalent (black curve, Fig. 8B). The difference between these two scenarios derives from varying the sensitivity of the ice sheet to warming through the melt parameter c_m. Next, we use a GIA model to predict RSL in The Bahamas (green curve, Fig. 8, see Materials and Methods), which shows that RSL closely tracks the ice-equivalent GMSL but can be up to 20% lower. This difference is smaller than the 30% difference obtained from the purely elastic fingerprint (Hay et al., 2014) because the onset of viscous deformation acts to reduce the fingerprint signal. Uncertainties in Earth structure lead to small (centimeter to decimeter scale) uncertainties in the predicted RSL signal in response to GrIS melt (green shading, Fig. 8), given that the total contribution of ice melt is on the order of meters. We then calculate the ice equivalent GMSL change not driven by GrIS melt by removing the RSL signal due to Greenland melt from our GMSL curve (red line, Fig. 8). This residual is caused by a combination of mountain glacier melt, thermal expansion, and Antarctic ice melt. Note that the modeled results of GrIS contribution to global sea level by Calov et al. (2015) are similar to models and proxy-based reconstructions of MIS 5e ice loss suggested by Bradley et al. (2018), Dahl-Jensen et al. (2013), Goelzer et al. (2016), Quiquet et al. (2013), most likely reaching peak contributions late in MIS 5e.

We estimate the ice equivalent sea-level change driven by water and steric sources other than the GrIS from our GMSL curve estimated using both closed-system (Fig. 8A) and open-system (Fig. 8B) ages. Since the results for the most likely GMSL curve are very similar between the two sets of ages over the entire span of MIS 5e, correcting our samples for open-system behavior does not impact the timing and trend of the GrIS and non-GrIS melt contributions. The resulting GMSL change, shown in blue, includes uncertainties driven by both the inferred GMSL and the Greenland-melt-driven sea-level signal. This remainder is a combination of mountain glacier melt, thermal expansion, and Antarctic ice melt (and its respective fingerprint). Mountain glaciers and thermal expansion possibly contributed around 30 cm of sea-level rise, each with uncertainties about the spatial distribution and temporal evolution of this signal (Farinotti et al., 2019; Hoffman et al., 2017). The elastic fingerprint of West Antarctic ice melt on RSL in The Bahamas is ~20%, meaning that RSL would overestimate the ice equivalent sea level by this amount. However, as shown by Hay et al. (2014) and our calculation for GrIS above, this deviation between GMSL and RSL is smaller when the viscous effects are included.

If the GrIS followed the first melt scenario (Fig. 8A), our results indicate that the remaining sea-level signal also varies by several meters but is asynchronous with the GrIS contribution. Given that mountain glaciers and thermal expansion only contribute small amounts to this signal, we conclude that this scenario would imply an out of phase contribution from the AIS with early melt from Antarctica, followed by AIS regrowth above its present volume while GrIS melt peaks at ~122 ka. Towards the end of the interglacial (~121-116 ka) the GrIS would be gaining mass while the AIS would experience renewed melting. In the second scenario (Fig. 8B), GrIS melt peaks at a much lower magnitude, which reduces the variability of the remaining sea-level signal. However, the variability in the non-GrIS contribution is still large enough that it would require an asynchronous AIS melt signal, though of lower amplitude than the first melt scenario. Assuming the remaining signal purely reflects AIS melt, this scenario would imply that AIS volume reached a minimum around 128-127 ka, then ice regrew until ~121 ka and finally AIS melting recommenced and lasted until ~118 ka before ice growth towards stage MIS-5d. These simulations are consistent with results from Rohling et al. (2019), but there is no agreement in the contribution magnitude.

In both GrIS scenarios, the non-GrIS sea-level component implied by the Bahamas data happens early in the interglacial and does not exceed ~3.5 m (97.5th percentile). This value is the same for both scenarios since neither predict any early melt from GrIS. We suggest that the majority of this signal would be caused by Antarctic ice melt possibly in response to stronger Southern Hemisphere summer high latitude insolation earlier in T-II (~136 ka). A significant contribution of AIS melting to the MIS 5e sea-level peak may have occurred during and following Heinrich Stadial 11 (~135-130 ka (Marino et al., 2015)), when Northern hemisphere ice sheet deglaciation caused a sustained reduction in Atlantic meridional overturning circulation that likely warmed the Southern Ocean (Clark et al., 2020; Turney et al., 2020). This massive meltwater injection to the North Atlantic initiated a bipolar see-saw temperature phenomenon, which could explain the asynchronicity of Antarctic and Greenland ice mass loss (Marino et al., 2015). The occurrence of this meltwater pulse reinforces the positive feedback described in Turney et al. (2020), which indicates substantial ice mass loss from Antarctica most likely in response to ocean warming early in the last interglacial, suggesting that AIS is highly sensitive to rising ocean temperatures.

Our results of a dominant early contribution from the Antarctic ice sheet are consistent with a recent study that used last interglacial sea level observations from Northwest Europe to fingerprint the contribution of the Antarctic ice sheet (Barnett et al., 2023). Barnett et al. (2023) found that the Antarctic ice sheet contributed approx. 2.5–8 m (1 sigma range) during the early MIS 5e, which is at the upper end of our estimates for this time range but overlaps with estimates used by DeConto et al. (2021) in Antarctic ice model calibrations. They predict that the Antarctic contribution declines towards the end of the MIS 5e to a minimum of −1 to 3 m in contrast to an Antarctic contribution that declines to a minimum and then increases again as we predict here. However, we emphasize again that details of our predictions (especially during the latter part of the MIS 5e) are predicated on a known Greenland ice history, which differs from the study by Barnett et al. (2023). We also note that if remnants of the Laurentide ice sheet persisted at the beginning of the MIS 5e (Zhou and McManus, 2022), it would imply an even smaller AIS during this time (in both our study and that by Barnett et al., 2023) to balance the excess ice in the northern hemisphere.

The two GrIS scenarios explored here serve to demonstrate how GrIS melt affects RSL in The Bahamas and what inferences could be drawn about the history of the Antarctic ice sheet if the GrIS melt component were well constrained. We acknowledge that the estimate of GrIS contribution between the different ice models varies in magnitude (from 0 to 5 m (Bradley et al., 2018; Goelzer et al., 2016; Quiquet et al., 2013; Yau et al., 2016)), however, the timing is relatively similar, indicating that our result of asynchronous behavior between the northern and southern hemisphere is robust (see Fig. S3). Reliable estimates of GIA-corrected sea level from locations across the globe will be necessary to jointly fingerprint the contributions from the Greenland and Antarctic ice sheets.

The inferred hemispheric melt scenarios shown in Fig. 7 have broader implications for future sea-level rise. The patterns imply that ice sheets are very sensitive to peaks in regional summer insolation (e.g.,

anti-phased at precession frequency). MIS 5e atmospheric CO_2 levels were similar to pre-industrial values, so the 1.5 °C globally averaged warming was primarily due to enhanced mid to high latitude insolation. On the other hand, as the Earth continues to warm due to anthropogenic greenhouse gas increases, warming at both poles will be synchronous. Thus, one might consider the possibility that the amplitude of the total future sea-level change would be equivalent to the summed (rather than antiphased) responses shown in Fig. 8. More importantly, this implies that using the GMSL estimates of MIS 5e as an analog for or to constrain sea-level projections of the future would likely lead to an underestimation of future sea-level rise.

4. Conclusions

We present a new collection of 23 high-precision U-series ages of MIS 5e corals from Crooked and Long Islands, Long Cay, and Eleuthera, in The Bahamas. We show that through strict sample screening we were able to obtain reliable U-series ages, with all but two samples falling within a narrow $\delta^{234}U_{initial}$ range between 143.8 and 151.3‰. Our analysis, which includes a probabilistic assessment of 579 distinct GIA models, results in a posterior GMSL curve which likely (68% probability) peaked higher than 1 m, but very unlikely (5% probability) exceeded 2.7 m, when using the open-system corrected ages, which we show are more likely than the closed-system ages to reflect the true ages. When closed-system ages are considered, the results for the most likely GMSL curve are very similar, but the range increases to 5.3 m. Whether open- or closed-system ages are used, our most likely GMSL curve is considerably lower than the previously-estimated peak MIS 5e GMSL range of 5–10 m above present. However, we show that our prediction is not necessarily inconsistent with sea level observations at other sites and consistent with other studies that have also recently yielded GMSL estimates less than 5 m (Clark et al., 2020; Dyer et al., 2021; Polyak et al., 2018). We highlight that the methodology pioneered by (Potter et al., 2004) for MIS5a and5c, used by Dyer et al. (2021) for MIS 5e, whereby geographical gradients in contemporaneous sea-level indicators are used to refine GIA corrections, which can also be applied in other regions of the world. This would allow the GMSL estimates proposed here to be further refined, especially when paired with high-quality U-series ages of carbonates.

We use this new GMSL estimate to investigate the timing and sources of meltwater contributions to MIS 5e sea level by analyzing different melt scenarios of GrIS to infer, by difference, the AIS melt contribution. Given our relatively constant GIA-corrected sea level in The Bahamas, we find that Northern and Southern Hemisphere ice sheets during MIS 5e melted beyond their present extent and either did not vary in size or, more likely given the insolation forcing, melted out-of-phase. In both scenarios of GrIS melt that we tested the AIS melts early, and then re-grows while the GrIS melts. AIS melt then commences again or speeds up when the GrIS contribution wanes. This may suggest that GrIS melt peaks at ~122 ka, which would increase GMSL, could cause a destabilization of marine-based sectors in Antarctica, leading to AIS retreat. Since MIS 5e warming was likely driven by insolation, which would have impacted each hemisphere at different times, our estimates indicate that individual ice sheets may still be very sensitive to regional temperature change. We acknowledge that existing estimates of the GrIS contribution are still uncertain; this highlights the need for additional reliable estimates of GMSL with tightly constrained chronologies from different locations to fingerprint the contribution from the Greenland and Antarctic ice sheet to MIS 5e GMSL.

Author contributions

B.D., J.A., W.J.D., O.A.D, and M.E.R. designed the study; B.D., J.A., W.J.D., R.C.C., M.R.S., M.C., and M.E.R. measured corals elevations and collected samples; S.L.G. and L.B. were responsible for the lab and instrumentation; O.A.D., S.L.G, L.B., M.R.S., and M.C. developed the measurement protocols and/or measured U–Th ages of coral samples; O. A.D. and S.L.G. evaluated U-series data quality and implications; B.D. performed the statistical analysis; J.A. performed GIA modeling including the fingerprint analysis; O.A.D., B.D., M.E.R., S.L.G, and J.A. interpreted data, drafted and wrote the majority of the manuscript with input from all authors.

Declaration of competing interest

The authors declare that they have no known competing financial interests or personal relationships that could have appeared to influence the work reported in this paper.

Data availability

"The relevant code, model input, and output will be available on Zenodo. The Bayesian inversion code and the GIA code will be available on GitHub. All U–Th data will be available on EarthChem. "https://data.elsevier.com/research/editorialmanager/researchdatadatapump.json.

Acknowledgments

This material is based upon work supported by NSF Grants OCE-1841888 and OCE-2103064. We thank The Bahamas Environment, Science & Technology Commission and many Bahamian people for support of our field work. TanDEM-X digital elevation data are under copyright by the German Aerospace Center. All rights reserved; used with permission within Project DEM GEOL1210 (A.R./M.E.R.). We also thank Reinhard Kozdon for the resources in the sample preparation laboratory. We acknowledge PALSEA, a working group of the International Union for Quaternary Sciences (INQUA) and Past Global Changes (PAGES), which in turn received support from the Swiss Academy of Sciences and the Chinese Academy of Sciences.

Appendix A. Supplementary data

Supplementary data to this article can be found online at https://doi.org/10.1016/j.quascirev.2023.108287.

References

Austermann, J., Hoggard, M.J., Latychev, K., Richards, F.D., Mitrovica, J.X., 2021. The effect of lateral variations in Earth structure on Last Interglacial sea level. Geophys. J. Int. 227, 1938–1960.
Austermann, J., Mitrovica, J.X., Huybers, P., Rovere, A., 2017. Detection of a dynamic topography signal in last interglacial sea-level records. Sci. Adv. 3, e1700457.
Barnett, R.L., Austermann, J., Dyer, B., Telfer, M.W., Barlow, N.L.M., Boulton, S.J., Carr, A.S., Creel, R.C., 2023. Constraining the contribution of the antarctic ice sheet to last interglacial sea level. Sci. Adv. 9 (27), eadf0198.
Berger, A., Loutre, M.F., 1991. Insolation values for the climate of the last 10 million years. Quat. Sci. Rev. 10, 297–317.
Berkeley, A., Rankey, E.C., 2012. Progradational Holocene carbonate tidal flats of Crooked Island, south-east Bahamas: an alternative to the humid channelled belt model. Sedimentology 59, 1902–1925.
Blanchon, P., Eisenhauer, A., Fietzke, J., Liebetrau, V., 2009. Rapid sea-level rise and reef back-stepping at the close of the last interglacial highstand. Nature 458, 881–884.
Bradley, S.L., Reerink, T.J., van de Wal, R.S.W., Helsen, M.M., 2018. Simulation of the Greenland Ice Sheet over two glacial–interglacial cycles: investigating a sub-ice-shelf melt parameterization and relative sea level forcing in an ice-sheet–ice-shelf model. Clim. Past 14, 619–635.
Caldwell, P., Merrifield, M., Thompson, P., 2015. Sea level measured by tide gauges from global oceans- the Joint Archive for Sea Level holdings. In: Dataset 10. V.V.S.W.V., NOAA National Centers for Environmental, Information, S.S., MD, 2015. NCEI Accession 0019568.
Calov, R., Robinson, A., Perrette, M., Ganopolski, A., 2015. Simulating the Greenland ice sheet under present-day and palaeo constraints including a new discharge parameterization. Cryosphere 9, 179–196.
Carew, J.L., Mylroie, J.E., 1995. Quaternary tectonic stability of the Bahamian Archipelago: evidence from fossil coral reefs and flank margin caves. Quat. Sci. Rev. 14, 144–153.
Carlton, R., Dempsey, A., Thompson, L., Heemsoth, A., Lubarsky, K., Faisal, M., Purkis, S., 2021. Global Reef Expedition Final Report. Khaled bin Sultan Living Oceans Foundation, Annapolis, MD.

Chen, J.H., Curran, H.A., White, B., Wasserburg, G.J., 1991. Precise chronology of the last interglacial period: 234U-230Th data from fossil coral reefs in the Bahamas. GSA Bulletin 103, 82–97.
Cheng, H., Lawrence Edwards, R., Shen, C.-C., Polyak, V.J., Asmerom, Y., Woodhead, J., Hellstrom, J., Wang, Y., Kong, X., Spötl, C., Wang, X., Calvin Alexander, E., 2013. Improvements in 230Th dating, 230Th and 234U half-life values, and U–Th isotopic measurements by multi-collector inductively coupled plasma mass spectrometry. Earth Planet Sci. Lett. 371–372, 82–91.
Chutcharavan, P.M., Dutton, A., 2021. A global compilation of U-series-dated fossil coral sea-level indicators for the Last Interglacial period (Marine Isotope Stage 5e). Earth Syst. Sci. Data 13, 3155–3178.
Chutcharavan, P.M., Dutton, A., Ellwood, M.J., 2018. Seawater 234U/238U recorded by modern and fossil corals. Geochem. Cosmochim. Acta 224, 1–17.
Clark, P.U., He, F., Golledge, N.R., Mitrovica, J.X., Dutton, A., Hoffman, J.S., Dendy, S., 2020. Oceanic forcing of penultimate deglacial and last interglacial sea-level rise. Nature 577, 660–664.
Cobb, K.M., Charles, C.D., Cheng, H., Kastner, M., Edwards, R.L., 2003. U/Th-dating living and young fossil corals from the central tropical Pacific. Earth Planet Sci. Lett. 210, 91–103.
Creveling, J.R., Mitrovica, J.X., Hay, C.C., Austermann, J., Kopp, R.E., 2015. Revisiting tectonic corrections applied to Pleistocene sea-level highstands. Quat. Sci. Rev. 111, 72–80.
Dahl-Jensen, D., Albert, M.R., Aldahan, A., Azuma, N., Balslev-Clausen, D., Baumgartner, M., Berggren, A.M., Bigler, M., Binder, T., Blunier, T., Bourgeois, J.C., Brook, E.J., Buchardt, S.L., Buizert, C., Capron, E., Chappellaz, J., Chung, J., Clausen, H.B., Cvijanovic, I., Davies, S.M., Ditlevsen, P., Eicher, O., Fischer, H., Fisher, D.A., Fleet, L.G., Gfeller, G., Gkinis, V., Gogineni, S., Goto-Azuma, K., Grinsted, A., Gudlaugsdottir, H., Guillevic, M., Hansen, S.B., Hansson, M., Hirabayashi, M., Hong, S., Hur, S.D., Huybrechts, P., Hvidberg, C.S., Iizuka, Y., Jenk, T., Johnsen, S.J., Jones, T.R., Jouzel, J., Karlsson, N.B., Kawamura, K., Keegan, K., Kettner, E., Kipfstuhl, S., Kjær, H.A., Koutnik, M., Kuramoto, T., Köhler, P., Laepple, T., Landais, A., Langen, P.L., Larsen, L.B., Leuenberger, D., Leuenberger, M., Leuschen, C., Li, J., Lipenkov, V., Martinerie, P., Maselli, O.J., Masson-Delmotte, V., McConnell, J.R., Miller, H., Mini, O., Miyamoto, A., Montagnat-Rentier, M., Mulvaney, R., Muscheler, R., Orsi, A.J., Paden, J., Panton, C., Pattyn, F., Petit, J.R., Pol, K., Popp, T., Possnert, G., Prié, F., Prokopiou, M., Quiquet, A., Rasmussen, S.O., Raynaud, D., Ren, J., Reutenauer, C., Ritz, C., Röckmann, T., Rosen, J.L., Rubino, M., Rybak, O., Samyn, D., Sapart, C.J., Schilt, A., Schmidt, A.M.Z., Schwander, J., Schüpbach, S., Seierstad, I., Severinghaus, J.P., Sheldon, S., Simonsen, S.B., Sjolte, J., Solgaard, A.M., Sowers, T., Sperlich, P., Steen-Larsen, H.C., Steffen, K., Steffensen, J.P., Steinhage, D., Stocker, T.F., Stowasser, C., Sturevik, A.S., Sturges, W.T., Sveinbjörnsdottir, A., Svensson, A., Tison, J.L., Uetake, J., Vallelonga, P., van de Wal, R.S.W., van der Wel, G., Vaughn, B.H., Vinther, B., Waddington, E., Wegner, A., Weikusat, I., White, J.W.C., Wilhelms, F., Winstrup, M., Witrant, E., Wolff, E.W., Xiao, C., Zheng, J., members, N.c., 2013. Eemian interglacial reconstructed from a Greenland folded ice core. Nature 493, 489–494.
DeConto, R.M., Pollard, D., 2016. Contribution of Antarctica to past and future sea-level rise. Nature 531, 591–597.
DeConto, R.M., Pollard, D., Alley, R.B., Velicogna, I., Gasson, E., Gomez, N., Sadai, S., Condron, A., Gilford, D.M., Ashe, E.L., Kopp, R.E., Li, D., Dutton, A., 2021. The Paris Climate Agreement and future sea-level rise from Antarctica. Nature 593, 83–89.
Dendy, S., Austermann, J., Creveling, J.R., Mitrovica, J.X., 2017. Sensitivity of Last Interglacial sea-level high stands to ice sheet configuration during Marine Isotope Stage 6. Quat. Sci. Rev. 171, 234–244.
Dutton, A., Carlson, A.E., Long, A.J., Milne, G.A., Clark, P.U., DeConto, R., Horton, B.P., Rahmstorf, S., Raymo, M.E., 2015. Sea-level rise due to polar ice-sheet mass loss during past warm periods. Science 349, aaa4019.
Dutton, A., Kerans, C., 2021. Sedimentologic, stratigraphic, and diagenetic evidence for an intra-MIS 5e sea level fall across the Bahamas-Caribbean region, PP52B-02.
Dutton, A., Lambeck, K., 2012. Ice volume and sea level during the last interglacial. Science 337, 216.
Dyer, B., Austermann, J., D'Andrea, W.J., Creel, R.C., Sandstrom, M.R., Cashman, M., Rovere, A., Raymo, M.E., 2021. Sea-level trends across the Bahamas constrain peak last interglacial ice melt. Proc. Natl. Acad. Sci. USA 118, e2026839118.
Dziewonski, A.M., Anderson, D.L., 1981. Preliminary reference Earth model. Phys. Earth Planet. In. 25, 297–356.
Farinotti, D., Huss, M., Fürst, J.J., Landmann, J., Machguth, H., Maussion, F., Pandit, A., 2019. A consensus estimate for the ice thickness distribution of all glaciers on Earth. Nat. Geosci. 12, 168–173.
Fischer, H., Meissner, K.J., Mix, A.C., Abram, N.J., Austermann, J., Brovkin, V., Capron, E., Colombaroli, D., Daniau, A.-L., Dyez, K.A., Felis, T., Finkelstein, S.A., Jaccard, S.L., McClymont, E.L., Rovere, A., Sutter, J., Wolff, E.W., Affolter, S., Bakker, P., Ballesteros-Cánovas, J.A., Barbante, C., Caley, T., Carlson, A.E., Churakova, O., Cortese, G., Cumming, B.F., Davis, B.A.S., de Vernal, A., Emile-Geay, J., Fritz, S.C., Gierz, P., Gottschalk, J., Holloway, M.D., Joos, F., Kucera, M., Loutre, M.-F., Lunt, D.J., Marcisz, K., Marlon, J.R., Martinez, P., Masson-Delmotte, V., Nehrbass-Ahles, C., Otto-Bliesner, B.L., Raible, C.C., Risebrobakken, B., Sánchez Goñi, M.F., Arrigo, J.S., Sarnthein, M., Sjolte, J., Stocker, T.F., Velasquez Alvárez, P.A., Tinner, W., Valdes, P.J., Vogel, H., Wanner, H., Yan, Q., Yu, Z., Ziegler, M., Zhou, L., 2018. Palaeoclimate constraints on the impact of 2 °C anthropogenic warming and beyond. Nat. Geosci. 11, 474–485.
Ocean, cryosphere and sea level change. In: Fox-Kemper, B., Hewitt, H.T., Xiao, C., Aðalgeirsdóttir, G., Drijfhout, S.S., Edwards, T.L., Golledge, N.R., Hemer, M., Kopp, R.E., Krinner, G., Mix, A., Notz, D., Nowicki, S., Nurhati, I.S., Ruiz, L., Sallée, J.-B., Slangen, A.B.A., Yu, Y., Masson-Delmotte, V., Zhai, P., Pirani, A., Connors, S.L., Péan, C., Berger, S., Caud, N., Chen, Y., Goldfarb, L., Gomis, M.I., Huang, M., Leitzell, K., Lonnoy, E., Matthews, J.B.R., Maycock, T.K., Waterfield, T., Yelekçi, O., Yu, R., Zhou, B. (Eds.), 2021. Climate Change 2021: the Physical Science Basis. Contribution of Working Group I to the Sixth Assessment Report of the Intergovernmental Panel on Climate Change United Kingdom and New York, NY, USA, pp. 1211–1362.
Garbe, J., Albrecht, T., Levermann, A., Donges, J.F., Winkelmann, R., 2020. The hysteresis of the antarctic ice sheet. Nature 585, 538–544.
Garrett, P., Gould, S.J., 1984. Geology of new providence island, Bahamas. GSA Bulletin 95, 209–220.
Gilford, D.M., Ashe, E.L., DeConto, R.M., Kopp, R.E., Pollard, D., Rovere, A., 2020. Could the last interglacial constrain projections of future antarctic ice mass loss and sea-level rise? J. Geophys. Res.: Earth Surf., e2019JF005418 n/a.
Godefroid, F., Kindler, P., 2015. Prominent geological features of crooked island, se Bahamas. In: The 16th Symposium on the Geology of the Bahamas and Other Carbonate Regions, pp. 26–38.
Goelzer, H., Huybrechts, P., Loutre, M.F., Fichefet, T., 2016. Last Interglacial climate and sea-level evolution from a coupled ice sheet–climate model. Clim. Past 12, 2195–2213.
Goreau, T.F., Goreau, N.I., 1973. The ecology of Jamaican coral reefs: II. Geomorphology, zonation and sedimentary phases. Bull. Mar. Sci. 23, 339–464.
Halley, R.B., Harris, P.M., 1979. Fresh-water cementation of a 1,000-year-old oolite. J. Sediment. Res. 49, 969–987.
Hay, C., Mitrovica, J.X., Gomez, N., Creveling, J.R., Austermann, J., Kopp, E., R, 2014. The sea-level fingerprints of ice-sheet collapse during interglacial periods. Quat. Sci. Rev. 87, 60–69.
Hearty, P.J., Hollin, J.T., Neumann, A.C., O'Leary, M.J., McCulloch, M., 2007. Global sea-level fluctuations during the Last Interglaciation (MIS 5e). Quat. Sci. Rev. 26, 2090–2112.
Hearty, P.J., Kindler, P., 1993a. New perspectives on Bahamian geology: san salvador island, Bahamas. J. Coast Res. 9, 577–594.
Hearty, P.J., Kindler, P., 1993b. An illustrated stratigraphy of the Bahama Islands: in search of a common origin. Bahamas J. Sci. 1, 28–45.
Hearty, P.J., Pascal, K., 1997. The stratigraphy and surficial geology of new providence and surrounding islands, Bahamas. J. Coast Res. 13, 798–812.
Henderson, G.M., Anderson, R.F., 2003. The U-series toolbox for paleoceanography. Rev. Mineral. Geochem. 52, 493–531.
Hibbert, F.D., Rohling, E.J., Dutton, A., Williams, F.H., Chutcharavan, P.M., Zhao, C., Tamisiea, M.E., 2016. Coral indicators of past sea-level change: a global repository of U-series dated benchmarks. Quat. Sci. Rev. 145, 1–56.
Hoffman, J.S., Clark, P.U., Parnell, A.C., He, F., 2017. Regional and global sea-surface temperatures during the last interglaciation. Science 355, 276–279.
Horton, B.P., Khan, N.S., Cahill, N., Lee, J.S.H., Shaw, T.A., Garner, A.J., Kemp, A.C., Engelhart, S.E., Rahmstorf, S., 2020. Estimating global mean sea-level rise and its uncertainties by 2100 and 2300 from an expert survey. npj Climate and Atmospheric Science 3, 18.
IPCC, 2013. Climate Change 2013: the Physical Science Basis. Contribution of Working Group I to the Fifth Assessment Report of the Intergovernmental Panel on Climate Change. Cambridge University Press, Cambridge, United Kingdom and New York, NY, USA.
Kendall, R.A., Mitrovica, J.X., Milne, G.A., 2005. On post-glacial sea level – II. Numerical formulation and comparative results on spherically symmetric models. Geophys. J. Int. 161, 679–706.
Kerans, C., Zahm, C., Bachtel, S.L., Hearty, P., Cheng, H., 2019. Anatomy of a late Quaternary carbonate island: constraints on timing and magnitude of sea-level fluctuations, West Caicos, Turks and Caicos Islands, BWI. Quat. Sci. Rev. 205, 193–223.
Kindler, P., Mylroie, J.E., Curran, H.A., Carew, J.L., Gamble, D.W., Rothfus, T.A., 2010. Geology of Central Eleuthera, Bahamas: A Field Trip Guide.
Kopp, R.E., Simons, F.J., Mitrovica, J.X., Maloof, A.C., Oppenheimer, M., 2009. Probabilistic assessment of sea level during the last interglacial stage. Nature 462, 863–867.
Lorscheid, T., Rovere, A., 2019. The indicative meaning calculator – quantification of paleo sea-level relationships by using global wave and tide datasets. Open Geospatial Data, Software and Standards 4, 10.
Marino, G., Rohling, E.J., Rodríguez-Sanz, L., Grant, K.M., Heslop, D., Roberts, A.P., Stanford, J.D., Yu, J., 2015. Bipolar seesaw control on last interglacial sea level. Nature 522, 197–201.
McNeill, D.F., 2005. Accumulation rates from well-dated late Neogene carbonate platforms and margins. Sediment. Geol. 175, 73–87.
Muhs, D.R., Simmons, K.R., Schumann, R.R., Schweig, E.S., Rowe, M.P., 2020. Testing glacial isostatic adjustment models of last-interglacial sea level history in the Bahamas and Bermuda. Quat. Sci. Rev. 233, 106212.
Mylroie, J.E., 2008. Late Quaternary sea-level position: evidence from Bahamian carbonate deposition and dissolution cycles. Quat. Int. 183, 61–75.
O'Leary, M.J., Hearty, P.J., Thompson, W.G., Raymo, M.E., Mitrovica, J.X., Webster, J. M., 2013. Ice sheet collapse following a prolonged period of stable sea level during the last interglacial. Nat. Geosci. 6, 796–800.
Obert, J.C., Scholz, D., Felis, T., Brocas, W.M., Jochum, K.P., Andreae, M.O., 2016. 230Th/U dating of Last Interglacial brain corals from Bonaire (southern Caribbean) using bulk and theca wall material. Geochem. Cosmochim. Acta 178, 20–40.
Pattyn, F., Ritz, C., Hanna, E., Asay-Davis, X., DeConto, R., Durand, G., Favier, L., Fettweis, X., Goelzer, H., Golledge, N.R., Kuipers Munneke, P., Lenaerts, J.T.M., Nowicki, S., Payne, A.J., Robinson, A., Seroussi, H., Trusel, L.D., van den Broeke, M., 2018. The Greenland and Antarctic ice sheets under 1.5 °C global warming. Nat. Clim. Change 8, 1053–1061.

Plach, A., Nisancioglu, K.H., Langebroek, P.M., Born, A., Le clec'h, S., 2019. Eemian Greenland ice sheet simulated with a higher-order model shows strong sensitivity to surface mass balance forcing. Cryosphere 13, 2133–2148.
Polyak, V.J., Onac, B.P., Fornós, J.J., Hay, C., Asmerom, Y., Dorale, J.A., Ginés, J., Tuccimei, P., Ginés, A., 2018. A highly resolved record of relative sea level in the western Mediterranean Sea during the last interglacial period. Nat. Geosci. 11, 860–864.
Potter, E.-K., Esat, T.M., Schellmann, G., Radtke, U., Lambeck, K., McCulloch, M.T., 2004. Suborbital-period sea-level oscillations during marine isotope substages 5a and 5c. Earth Planet Sci. Lett. 225, 191–204.
Quiquet, A., Ritz, C., Punge, H.J., Salas y Mélia, D., 2013. Greenland ice sheet contribution to sea level rise during the last interglacial period: a modelling study driven and constrained by ice core data. Clim. Past 9, 353–366.
Raymo, M.E., Mitrovica, J.X., O'Leary, M.J., DeConto, R.M., Hearty, P.J., 2011. Departures from eustasy in Pliocene sea-level records. Nat. Geosci. 4, 328–332.
Rohling, E.J., Hibbert, F.D., Grant, K.M., Galaasen, E.V., Irvalı, N., Kleiven, H.F., Marino, G., Ninnemann, U., Roberts, A.P., Rosenthal, Y., Schulz, H., Williams, F.H., Yu, J., 2019. Asynchronous Antarctic and Greenland ice-volume contributions to the last interglacial sea-level highstand. Nat. Commun. 10, 5040.
Sandstrom, R.M., 2021. Geochronology and Reconstruction of Quaternary and Neogene Sea-Level Highstands. Columbia University, Academic Commons.
Scholz, D., Mangini, A., 2007. How precise are U-series coral ages? Geochem. Cosmochim. Acta 71, 1935–1948.
Shinn, E.A., Lloyd, R.M., Ginsburg, R.N., 1969. Anatomy of a modern carbonate tidal-flat, Andros Island, Bahamas. J. Sediment. Res. 39.
Skrivanek, A., Li, J., Dutton, A., 2018. Relative sea-level change during the Last Interglacial as recorded in Bahamian fossil reefs. Quat. Sci. Rev. 200, 160–177.
Slater, T., Hogg, A.E., Mottram, R., 2020. Ice-sheet losses track high-end sea-level rise projections. Nat. Clim. Change 10, 879–881.
Stirling, C.H., Andersen, M.B., 2009. Uranium-series dating of fossil coral reefs: extending the sea-level record beyond the last glacial cycle. Earth Planet Sci. Lett. 284, 269–283.
Stocchi, P., Vacchi, M., Lorscheid, T., de Boer, B., Simms, A.R., van de Wal, R.S.W., Vermeersen, B.L.A., Pappalardo, M., Rovere, A., 2018. MIS 5e relative sea-level changes in the Mediterranean Sea: contribution of isostatic disequilibrium. Quat. Sci. Rev. 185, 122–134.
Thompson, W.G., Allen Curran, H., Wilson, M.A., White, B., 2011. Sea-level oscillations during the last interglacial highstand recorded by Bahamas corals. Nat. Geosci. 4, 684–687.
Thompson, W.G., Goldstein, S.L., 2005. Open-system coral ages reveal persistent suborbital sea-level cycles. Science 308, 401–404.
Thompson, W.G., Spiegelman, M.W., Goldstein, S.L., Speed, R.C., 2003. An open-system model for U-series age determinations of fossil corals. Earth Planet Sci. Lett. 210, 365–381.
Turney, C.S.M., Fogwill, C.J., Golledge, N.R., McKay, N.P., van Sebille, E., Jones, R.T., Etheridge, D., Rubino, M., Thornton, D.P., Davies, S.M., Ramsey, C.B., Thomas, Z.A., Bird, M.I., Munksgaard, N.C., Kohno, M., Woodward, J., Winter, K., Weyrich, L.S., Rootes, C.M., Millman, H., Albert, P.G., Rivera, A., van Ommen, T., Curran, M., Moy, A., Rahmstorf, S., Kawamura, K., Hillenbrand, C.-D., Weber, M.E., Manning, C. J., Young, J., Cooper, A., 2020. Early Last Interglacial ocean warming drove substantial ice mass loss from Antarctica. Proc. Natl. Acad. Sci. USA 117, 3996–4006.
Yau, A.M., Bender, M.L., Robinson, A., Brook, E.J., 2016. Reconstructing the last interglacial at summit, Greenland: insights from GISP2. Proc. Natl. Acad. Sci. USA 113, 9710.
Zhou, Y., McManus, J., 2022. Extensive evidence for a last interglacial Laurentide outburst (LILO) event. Geology 50 (8), 934–938.